Journal of Thermal Biology 134 (2025) 104343

Contents lists available at ScienceDirect

Journal of Thermal Biology

journal homepage: www.elsevier.com/locate/jtherbio

Comparative analysis of heat transfer and thermal damage of living biological tissue incorporating local thermal non-equilibrium, dual-phase-lags, and bioheat equations

Vannakorn Mongkol [a,c], Phadungsak Rattanadecho [a], Wutipong Preechaphonkul [b], Kambiz Vafai [c,*]

[a] Hub of Talents Electromagnetic Energy in Medical Engineering, Department of Mechanical Engineering, Faculty of Engineering, Thammasat University, (Rangsit Campus), 99 moo 18, Klong Luang, Pathum Thani, 12120, Thailand
[b] Institute of Field Robotics, King Mongkut's University of Technology, Thonburi, Bangkok, Thailand
[c] Department of Mechanical Engineering, Faculty of Engineering, University of California, A363 Bourns Hall, Riverside, CA 2507-0425, USA

ARTICLE INFO

Keywords:
Hyperthermia
Non-equilibrium
Dual-phase lag
Porous medium
Bioheat
Ablation

ABSTRACT

This study comparatively investigates three bioheat transfer models: the Pennes bioheat (PBH), the generalized dual-phase-lag model (DPL), and the local thermal non-equilibrium (LTNE) models to analyze heat transfer and thermal damage during microwave ablation (MWA). The effects of porosity, coupling factor, phase-lag time, heating duration, and blood velocity were investigated, and an axisymmetric model was employed for validation against experimental data. Results indicate that porosity and phase-lag time strongly influence the DPL framework, where higher porosity enhances convective cooling. In contrast, the PBH model exhibits a temperature trend similar to that of the LTNE model at moderate porosity levels. The comparison shows that the PBH model produced RMSE values of 5.98 °C and 3.04 °C (percentage errors of 14.89 % and 57.71 %) with a smaller ablation zone of −24.47 %, while the DPL model exhibited the largest deviations, with RMSE values of 17.67 °C and 8.32 °C (percentage errors of 41.84 % and 237.92 %) and a smaller ablation zone of −65.57 %. In contrast, the LTNE model achieved the best agreement with experimental data, yielding RMSE values of 1.16 °C and 0.90 °C at 1 cm and 2 cm (percentage errors of 3.14 % and 17.05 %) with a slightly larger ablation zone of +17.25 %. These findings confirm that the LTNE framework most accurately predicts temperature evolution and ablation behavior, while highlighting the need to incorporate dynamic blood flow, tissue shrinkage, and mechanical deformation to improve physiological realism and enhance predictive capability for clinical hyperthermia applications.

1. Introduction

Modeling heat transport in biological tissues is crucial for designing, controlling, and optimizing thermal therapeutic applications, such as hyperthermia (Suriyanto et al., 2017), hypothermia (Silva et al., 2018), microwave ablation (MWA) (Tucci et al., 2022), laser ablation (LA) (Singh and Melnik, 2020), radiofrequency ablation (RFA) (Shao et al., 2017a,b), and high-intensity focused ultrasound (HIFU) (Namakshenas and Mojra, 2020). In modern medical applications, microwave ablation (MWA) has been extensively utilized for treating tumors in organs such as the liver, lungs, and breast due to its capability to generate rapid and high-intensity heating within a short duration (Namakshenas et al., 2024; Wessapan et al., 2025). Compared with laser ablation (LA), which is limited by its shallow penetration depth, and high-intensity focused ultrasound (HIFU), which provides noninvasive treatment but relatively slower heating rates, MWA enables more localized and deeper energy deposition through antenna insertion. Furthermore, MWA delivers higher power than radiofrequency ablation (RFA), resulting in larger ablation zones within shorter treatment times. However, the effectiveness of these treatments depends on precise control of temperature distribution and thermal damage to selectively ablate target tissue while preserving surrounding healthy regions. Therefore, mathematical modeling provides a powerful alternative for predicting and optimizing therapeutic outcomes. The Pennes bioheat (PBH) model (Pennes, 1948)

* Corresponding author.
E-mail address: vafai@ucr.edu (K. Vafai).

https://doi.org/10.1016/j.jtherbio.2025.104343
Received 1 October 2025; Received in revised form 26 November 2025; Accepted 27 November 2025
Available online 29 November 2025

is the most widely used framework, introducing a perfusion-based term to represent heat exchange between tissue and blood due to its simplicity and ease of implementation. However, it relies on idealized assumptions of uniform perfusion and instantaneous thermal equilibrium. To improve its accuracy, several extensions have been proposed, incorporating directional blood flow (Klinger, 1974; Wulff, 2007), countercurrent heat exchange (Mitchell and Myers, 1968; Weinbaum et al., 1984), effective perfusion (Shao et al., 2017b; Reis et al., 2016), and discrete vasculature (Kotte et al., 1999). Furthermore, Yang et al. (2007) enhanced the PBH model by including water evaporation effects during thermal ablation, achieving better agreement with experimental results.

Given the complex microvascular structure of biological tissues, modeling heat and fluid transport using porous media theory provides a more realistic alternative to traditional PBH-based formulations. In this framework, tissues are treated as two-phase systems consisting of a solid matrix (tissue) and a fluid phase (blood), allowing explicit representation of blood convection and vascular heat exchange (Roetzel and Xuan, 1998). Porous media models also enable coupling with flow and mass-transfer analyses, enhancing physiological realism in thermal simulations (Amiri and Vafai, 1994; Alazmi and Vafai, 2000; Khaled and Vafai, 2003; Khanafer et al., 2007; Iasiello et al., 2016; Wessapan and Rattanadecho, 2023). The local thermal equilibrium (LTE) model, assuming identical temperatures in both phases, has been widely applied (Rattanadecho and Keangin, 2013; Iasiello et al., 2020; Chabuanoi et al., 2024; Wessapan et al., 2025). However, the LTE assumption becomes unreliable in regions with large vessels or rapid thermal transients (Yuan, 2008). To overcome this limitation, the local thermal non-equilibrium (LTNE) model introduces separate energy equations for tissue and blood phases, enabling independent temperature evolution and interfacial heat transfer (Nakayama and Kuwahara, 2008; Mahjoob and Vafai, 2009; Keangin et al., 2013). Numerous studies have confirmed that parameters such as porosity, blood velocity, and vessel diameter strongly influence heat transfer, underscoring the suitability of LTNE-based models for predicting thermal responses in LA, MWA, and HIFU (Dombrovsky et al., 2012; Wang et al., 2015; Mohammadpour and Firoozabadi, 2020; Andreozzi et al., 2021; Iasiello et al., 2023; Imanlou and Vafai, 2025). In porous biological media, natural convection driven governs local heat redistribution between the solid tissue and blood phases. Similar behavior has been observed in porous flow systems, where thermal dispersion enhances convective heat transfer and energy transport (Abbas et al., 2009). Moreover, during microwave ablation (MWA), electromagnetic fields can further influence this convective mechanism, as demonstrated in magnetohydrodynamic flow studies where magnetic fields modify fluid motion and reduce convective heat transport (Abbas and Palani, 2010). Overall, porous media modeling provides a physiologically realistic framework by capturing tissue–blood interactions and blood flow during hyperthermia treatment.

Nonetheless, PBH and porous media models, including LTE and LTNE, are based on Fourier's law, which assumes infinite heat propagation speed, an unrealistic condition under short or intense heating such as laser pulses (Banerjee et al., 2005). To address this, the dual phase lag (DPL) model introduces relaxation times for heat flux and temperature gradient, enabling finite-speed conduction and delayed thermal response. Experiments have shown that the DPL model better captures transient temperature behavior during rapid heating (Mitra et al., 1995; Antaki, 2005). Analytical investigations based on the phase lag model have demonstrated that incorporating these lag parameters significantly improves transient temperature prediction and reduces the overestimation of thermal damage compared with the classical bioheat formulation (Ghanmi and Abbas, 2019). Furthermore, the relaxation time of heat flux was reported to be approximately 3–3.5 s, confirming the existence of delayed heat-transfer behavior in biological tissue under laser irradiation and showing good agreement with experimental data (Alzahrani and Abbas, 2019; Hobiny and Abbas , 2020; Abbas et al., 2020). The effects of the single-phase-lag (SPL), dual-phase-lag (DPL), and three-phase-lag (TPL) models were also investigated by Hobiny et al. (2020) and Alzahrani and Abbas (2021), showing that the DPL and TPL formulations reduce the peak temperature rise and yield temperature profiles that closely align with experimental results compared with the SPL model, which incorporates only the phase-lag time of heat flux. Moreover, the studies demonstrated that the blood perfusion rate significantly influences heat transfer in biological tissue by altering both the temperature distribution and the extent of thermal damage.

Recent analytical developments have extended the phase-lag framework to incorporate thermomechanical coupling and non-Fourier effects. Hobiny and Abbas (2023) and Abbas et al. (2024) employed generalized thermo-mechanical and biothermoelastic models with a single thermal relaxation time to analyze the coupled thermal and mechanical behavior of biological tissues under laser heating. Both studies demonstrated that increasing the relaxation time or blood perfusion rate reduces the peak temperature, stress, strain, and tissue deformation, confirming the strong coupling between heat transfer and mechanical response in biological media. These findings further highlight the versatility of phase-lag–based models, which can be effectively applied to analyze complex Multiphysics phenomena.

Later, Zhang (2009) introduced a generalized dual-phase-lag (DPL) model for bioheat transfer under local thermal non-equilibrium (LTNE) conditions. In this model, thermal relaxation time depends on porosity, thermophysical properties, and blood perfusion rate. Subsequent studies have emphasized the significant role of phase lag in thermal therapies (Zhou et al., 2009; Tzou, 2014; Kumar et al., 2015; Liu and Chen, 2015; Namakshenas and Mojra, 2021; Preechaphonkul et al., 2025b). Zhang et al. (2021) further examined the effects of physiological properties and phase lag on thermal and mechanical behavior during laser heating, while Zeinali et al. (2024) demonstrated that the generalized DPL model predicts different damage patterns compared with the classical formulation in HIFU simulations. More recently, Boontatao et al. (2025) applied the generalized DPL framework to prostate laser therapy, analyzing the influence of hyaluronic acid, collagen, and balloon spacers. These studies confirm that the generalized DPL model remains a robust and widely adopted tool in modern biomedical heat transfer simulations.

Although several bioheat transfer models have been proposed, their effectiveness in predicting temperature distribution and thermal damage during hyperthermia remains unclear. Most previous studies examined individual models under limited physiological or thermal conditions without systematic comparison across modeling frameworks. This gap creates uncertainty regarding the most suitable model for accurately representing heat transfer in biological tissues. Moreover, the combined effects of porosity, blood velocity, coupling factors, and relaxation times on tissue thermoregulation have not been comprehensively analyzed within a unified framework. To address these limitations, this study systematically compares three representative models: the Pennes bioheat (PBH), generalized dual-phase-lag (DPL), and local thermal non-equilibrium (LTNE) models to evaluate their predictive accuracy, parameter sensitivity, and agreement with experimental data. All models were implemented as one-dimensional axisymmetric simulations in COMSOL Multiphysics and validated against analytical solutions from Liu and Chen (2015), Zeinali et al. (2024), and Mahjoob and Vafai (2009).

The study comprises two main parts, as illustrated in Fig. 1(b). First, the sensitivity of each model to key parameters, including porosity, relaxation times, coupling factors, and blood velocity, was evaluated under identical conditions. Second, the models were validated against experimental microwave ablation (MWA) data from Namakshenas et al. (2024), representing realistic clinical conditions. The microwave heat source was adopted from the liver MWA model of Keangin and Rattanadecho (2013). Validation involved quantitative comparison of temperature profiles, ablation axes, and computation of Root Mean Square Error (RMSE) and relative error to assess agreement between simulations and experimental data. The findings clarify the strengths and limitations of each modeling approach, enabling more accurate

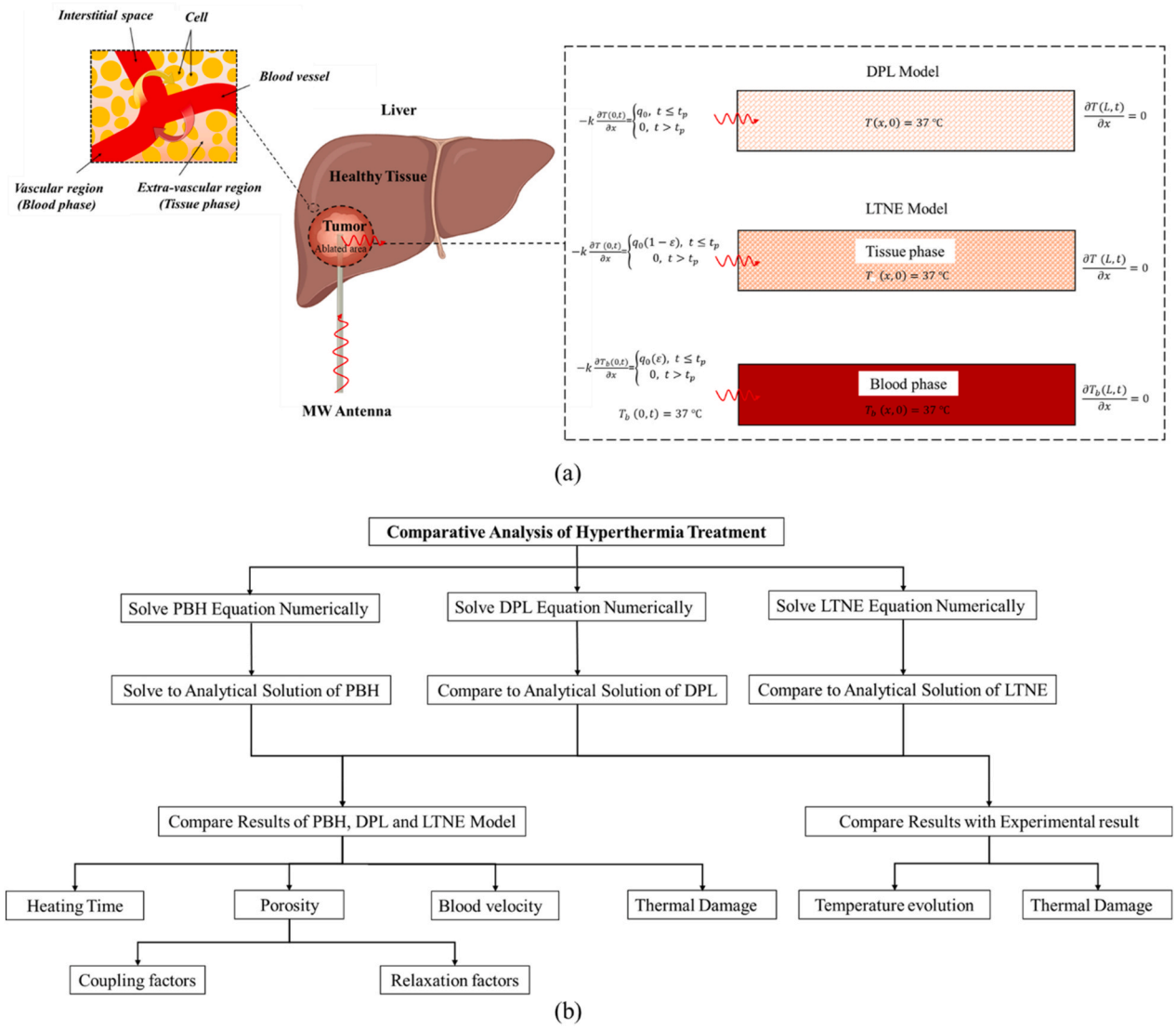

Fig. 1. (a) Schematic of MW-induced thermal ablation highlighting the porous structure of liver tissue, the LTNE model, and boundary conditions for heat transfer analysis; created with BioRender (biorender.com), and (b) a flowchart of the research steps.

prediction of thermal damage and reducing risk to surrounding healthy tissue. Furthermore, the results provide evidence-based guidance for thermal therapy design and a foundation for future model refinement.

2. Methods

2.1. Mathematical models

In this study, heat transfer in biological tissue was described using three models: the Pennes bioheat model (PBH), the generalized dual-phase-lag model (DPL), and the local thermal non-equilibrium model (LTNE). To reduce computational complexity while capturing the essential thermal behavior, the following assumptions were applied:

1. The heat transfer was modeled in a one-dimensional geometry.
2. Tissue properties were homogeneous, isotropic, and constant.
3. Water evaporation was neglected in Sections 3.2–3.5 due to short heating time and sub-evaporating temperatures, but was included in Section 3.6 because prolonged heating can elevate tissue temperature over 100 °C, where evaporation becomes significant.
4. Blood perfusion rate was considered constant in the PBH and DPL models.
5. Blood velocity was assumed to be constant in the LTNE model.
6. Mechanical deformation, including tissue shrinkage and thermal denaturation, was neglected.

2.1.1. The Pennes bioheat model (PBH model)

Heat transfer in biological tissue was introduced by Pennes (1948) incorporating blood perfusion and metabolic heat generation to represent the effects of blood flow in small capillaries and local metabolic heat sources within the tissue. The governing bioheat equation is expressed as follows:

$$\rho C\frac{\partial T}{\partial t} = \nabla\cdot(k\nabla T) + \rho_b C_b \omega_b (T_b - T) + Q_{met} + Q_{ext}, \quad (1)$$

where k, ρ, and C denote the conductivity, density, specific heat capacity of tissue. ρ_b, C_b, ω_b, and T_b are blood density, specific heat capacity of blood, blood perfusion rate, and blood temperature, Q_{met} is metabolic heat generation and Q_{ext} is term external heat sources.

2.1.2. The generalized dual-phase-lag model (DPL model)

The generalized dual-phase-lag model (DPL) proposed by Zhang (2009), formulated within the local thermal non-equilibrium (LTNE)

framework, is expressed in Eq. (2). In this model, the Phase lag of temperature gradient (τ_T) and heat flux (τ_q) are incorporated to describe heat transfer in biological tissue. These phase lag terms are influenced by blood and tissue properties, perfusion rate, and convective heat exchange between blood and surrounding cells (Liu and Chen, 2015; Zeinali et al., 2024).

$$\left(1+\tau_q\frac{\partial}{\partial t}\right)(\rho c)_{eff}\frac{\partial T}{\partial t}=\left(1+\tau_T\frac{\partial}{\partial t}\right)\left(k_{eff}\nabla^2 T\right)+G(T_b-T)+\left(1+\frac{\varepsilon\rho_b C_b}{G}\frac{\partial}{\partial t}\right)\left[(1-\varepsilon)Q_{met}+Q_{ext}\right], \tag{2}$$

where

$$(\rho c)_{eff}=\varepsilon\rho_b C_b+(1-\varepsilon)\,\rho c, \tag{3}$$

and

$$k_{eff}=\varepsilon k_b+(1-\varepsilon)\,k, \tag{4}$$

are effective heat capacity and thermal conductivity, respectively. $G=h_b a_b+\rho_b C_b\omega_b$ is coupling factor. τ_q and τ_T are phase lag of heat flux and temperature gradient, respectively. The phase lag times of the living biological tissues are estimated by Eqs. (5) and (6).

$$\tau_q=\frac{\varepsilon(1-\varepsilon)}{[\varepsilon/C_{sb}+(1-\varepsilon)]}\frac{\rho_b C_b}{G}, \tag{5}$$

$$\tau_T=\frac{\varepsilon(1-\varepsilon)}{[\varepsilon/k_{sb}+(1-\varepsilon)]}\frac{\rho_b C_b}{G}, \tag{6}$$

where

$$C_{sb}=\rho C\,/\,(\rho_b C_b), \tag{7}$$

$$k_{sb}=k/k_b, \tag{8}$$

are the ratios of heat capacities and thermal conductivities of tissue and blood.

2.1.3. The local thermal non equilibrium model (LTNE model)

The porous tissue model in the LTNE framework was represented by two distinct phases: the fluid-phase vascular region and the solid-phase extravascular region. Since the temperatures of blood and tissue in biological systems are generally not identical, the assumption of local thermal equilibrium (LTE) becomes inappropriate. Although the Pennes bioheat equation accounts for both tissue and blood temperatures, it simplifies the analysis by assuming that the blood temperature remains constant. During hyperthermia, the blood temperature changes due to convective heat exchange with the surrounding tissues. Accordingly, the local governing equations must be separately applied to the tissue and blood phases, resulting in a two-temperature model. The corresponding equations in which tissue and blood are modeled independently are as follows (Roetzel and Xuan, 1998; Nakayama and Kuwahara, 2008; Yuan, 2008; Mahjoob and Vafai, 2009):

Tissue phase:

$$(1-\varepsilon)\rho c\frac{\partial T}{\partial t}=(1-\varepsilon)k\nabla^2 T-h_b a_b(T-T_b)+(1-\varepsilon)Q_{met}+(1-\varepsilon)Q_{ext}, \tag{9}$$

Blood phase:

$$\varepsilon\rho_b c_b\left[\frac{\partial T_b}{\partial t}+V\cdot\nabla T_b\right]=\varepsilon k_b\nabla^2 T_b+h_b a_b(T-T_b)+\varepsilon Q_{ext}, \tag{10}$$

where ε are porosity, d_b is vascular diameter, h_b and a_b denote convective heat coefficient and specific area of blood vessel in tissue, respectively. The convective heat transfer coefficient and specific area in vessel can represent as $a_b=4\varepsilon/d_b$ (Roetzel and Xuan, 1998; $h_b=Nu\left(\frac{k_b}{d_b}\right)$ Nakayama and Kuwahara, 2008$h_b=Nu\left(\frac{k_b}{d_b}\right)$), respectively. Nu defines as the Nusselt number, which assumes to be 4.93 (Roetzel and Xuan, 1998; Tien and Vafai, 1989).

2.2. Boundary and initial conditions

The boundary conditions for the Pennes bioheat model (PBH) and the generalized dual-phase-lag model (DPL) are given in Eqs. (11) and (12), respectively, whereas the boundary conditions for the local thermal non-equilibrium (LTNE) model are presented in Eq. (13)–(17) as shown in Fig. 1(a).

2.2.1. Boundary conditions for PBH and DPL models

$$\text{At } x=0,\ -k\frac{\partial T}{\partial x}=\begin{cases} q_0 & t\le t_p \\ 0 & t>t_p \end{cases}. \tag{11}$$

$$\text{At } x=L,\ -k\frac{\partial T}{\partial x}=0. \tag{12}$$

2.2.2. Boundary conditions for LTNE model

Tissue phase:

$$\text{At } x=0,\ -k\frac{\partial T}{\partial x}=\begin{cases} (1-\varepsilon)q_0, & t\le t_p \\ 0\ , & t>t_p \end{cases}. \tag{13}$$

$$\text{At } x=L,\ -k\frac{\partial T}{\partial x}=0. \tag{14}$$

Blood phase:

$$\text{At } x=0,\ -k_b\frac{\partial T_b}{\partial x}=\begin{cases} \varepsilon q_0, & t\le t_p \\ 0\ , & t>t_p \end{cases}. \tag{15}$$

$$\text{At } x=0, T_b=37\ ^\circ C. \tag{16}$$

$$\text{At } x=L,\ -k_b\frac{\partial T_b}{\partial x}=0. \tag{17}$$

The initial temperature blood and tissue and was set to 37 $^\circ C$.

2.3. Thermal damage analysis

To explain the structural changes in tissue caused by protein degradation during thermal ablation, tissue damage was evaluated using the following Arrhenius damage equation (Andreozzi et al., 2019, 2021, 2022; Tucci et al., 2021; Zeinali et al., 2024; Preechaphonkul et al., 2025a).

$$\frac{d\Omega}{dt}=A\exp\left(\frac{-E_a}{RT}\right), \tag{18}$$

here, Ω represents the cumulative tissue damage, A is the frequency factor, which equals 7.39×10^{39} (1/s), E_a denotes the activation energy, set at 2.577×10^{5} (J/mol), and R is the universal gas constant (J/mol K) (Zeinali et al., 2024).

The fraction of necrotic tissue (θ_d) can be mathematically expressed as:

$$\theta_d=1-\exp(-\Omega), \tag{19}$$

where θ_d ranges from 0 to 1, where 1 indicates complete tissue damage.

2.4. Calculation procedure

To analyze the thermal response of biological tissue during hyperthermia therapy, numerical simulations were conducted using COMSOL Multiphysics™. The Pennes bioheat equation was solved using the bioheat transfer interface in the heat transfer module, whereas the LTNE

equations were implemented using the heat transfer in solids and heat transfer in fluids interfaces to represent the tissue and blood phases, respectively. The DPL model was constructed within the PDE (coefficient form) interface in the mathematics module to explicitly define the governing equations and phase lag terms. The temperature variables in each governing equation were defined separately for their respective domains to ensure parameter distinction. The phase lag times (τ_q and τ_T) and coupling factor (G) were defined as user-specified variables.

All simulations were solved using a fully coupled, time-dependent solver with the PARDISO linear solver. The maximum number of iterations was set to 30. The maximum time step was determined from a time-step analysis, as presented in Table 3. Hence, the initial time step was set to 1×10^{-4} s, and the automatic time-stepping algorithm was allowed to increase up to 0.1 s as the maximum time step, with a relative tolerance of 1×10^{-6}. This adaptive time-stepping approach ensures both computational efficiency and temporal accuracy. A mesh convergence test was also performed, as presented in Table 4, and the optimal element size was found to be 1×10^{-4} m. In this study, the temperature–time data were recorded at 0.1-s intervals throughout each simulation. To investigate different scenarios, the time-dependent study

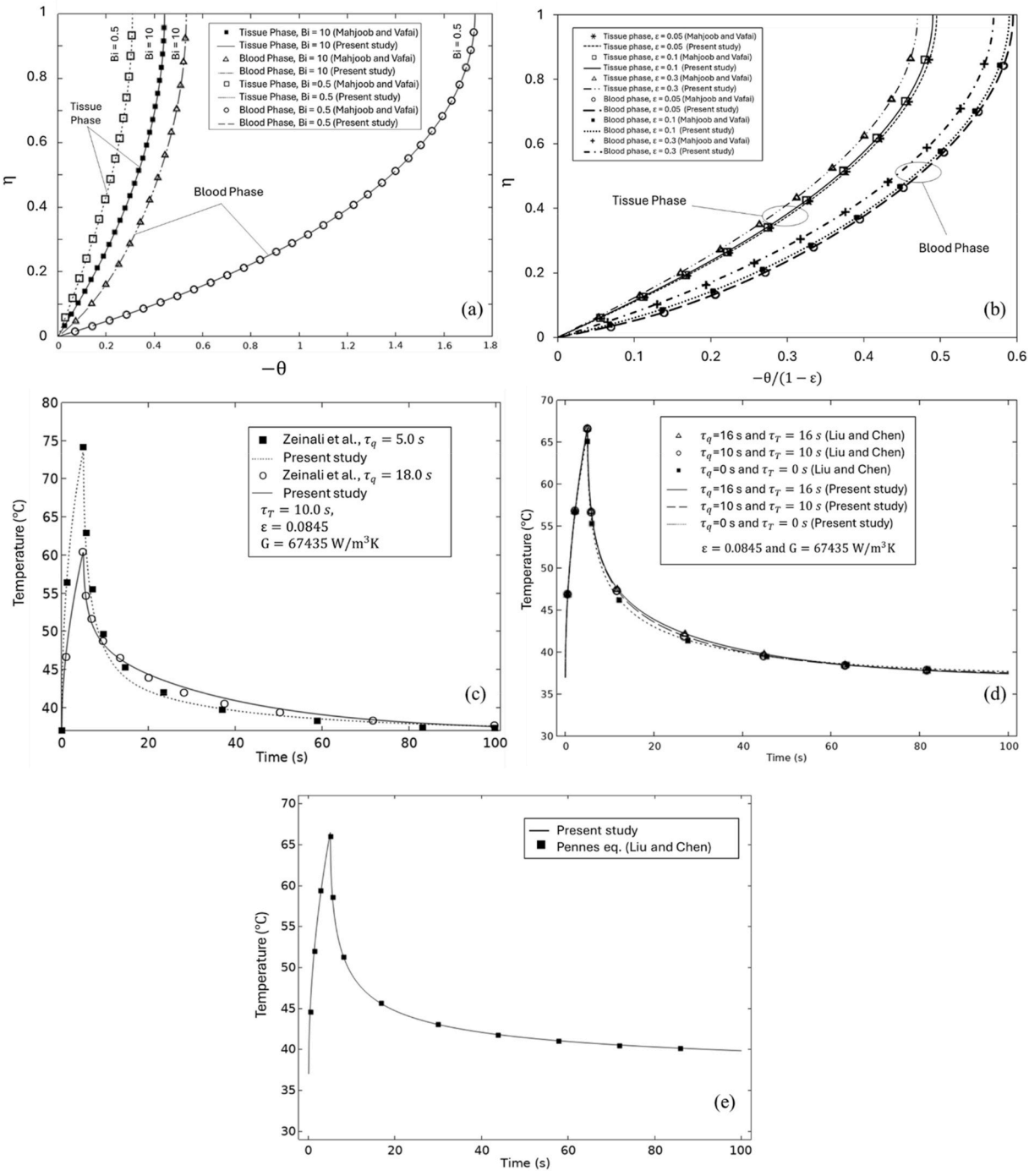

Fig. 2. (a–b) Comparison of the tissue and blood temperature profiles obtained from the present numerical results with the analytical results of Mahjoob and Vafai (2009) for the LTNE model, (c–d) comparison of temperature profiles obtained from the present numerical results with the analytical solutions reported by Zeinali et al. (2024) and Liu and Chen (2015) for the DPL model, and (e) comparison of temperature profiles obtained from the present numerical results with the analytical solution of Liu and Chen (2015) for the PBH model.

extension was applied. Simulations were performed using all combinations of tissue porosities (ε) (0.0079, 0.0845, 0.1437, and 0.2165) with blood velocities (V) of 0.1 mm/s and 1 mm/s, and heating durations (t_p) of 5 s and 20 s.

3. Results and discussion

3.1. Model verification

To verify the reliability of the present simulations, the three bioheat models (PBH, DPL, and LTNE) were individually validated against analytical solutions and experimental temperature data reported in previous studies. This separate validation ensures that the accuracy and predictive capability of each model can be independently evaluated. The LTNE model was validated against the analytical solutions of Mahjoob and Vafai (2009) to assess its reliability and accuracy. The dimensionless temperatures of tissue and blood for $\varepsilon = 0.1$, $\kappa = 0.111$, and $Bi = 0.5$ and 10 are shown in Fig. 2(a). Furthermore, Fig. 2(b) illustrates the influence of porosity ($\varepsilon = 0.05$, 0.1, and 0.3) on the dimensionless temperature profiles of tissue and blood under the conditions $-\theta/(1-\varepsilon) = 0.022$, $\kappa = 0.111$, and $Bi = 10$, consistent with the literature. The results demonstrate excellent agreement between the present numerical predictions and the analytical solutions of Mahjoob and Vafai (2009). In this context, the Biot number (Bi) represents the ratio of convective heat transfer by blood in the microvascular space to conductive heat transfer within the tissue. A lower Biot number (Bi = 0.5) produced larger deviations between tissue and blood temperatures than a higher value (Bi = 10), reflecting reduced heat exchange in sparsely vascularized tissue. Moreover, porosity, which characterizes the density of the microvascular network in biological media, plays a critical role in heat transfer under LTNE conditions. A reduction in porosity further amplifies the temperature difference between tissue and blood, emphasizing the physiological importance of porosity in regulating heat transport within biological tissue.

Similarly, the present DPL model was validated against the analytical solutions reported by Zeinali et al. (2024) and Liu and Chen (2015), as shown in Fig. 2(c and d), respectively. Fig. 2(c) compares the temperature profiles obtained from the current model with those of Zeinali et al. for $\tau_q = 5$ s and 18 s, $\tau_T = 10$ s, $\varepsilon = 0.0845$, and $G = 67435\ \mathrm{W/m^3K}$. In addition, Fig. 2(d) illustrates the comparison between the present results and Liu and Chen (2015)'s data using the DPL model for $\tau_q = \tau_T$ (0, 10, 16 s). It demonstrates good agreement with the analytical solutions. These validation results confirm the reliability of the present numerical model, showing excellent consistency with the established analytical data in the literature. It also demonstrates the effect of phase-lag on temperature rise in biological tissue. Specifically, increasing the phase-lag of heat flux (τ_q) reduces the rate of heat transfer, which in turn slows down the temperature rise of the tissue. Furthermore, the comparisons for identical phase-lag times (0, 10, and 16 s) reveal that larger phase-lag values are associated with slower temperature decay, highlighting the critical role of phase-lag in shaping the thermal response within the DPL framework. Lastly, the PBH model was also validated against the analytical results reported by Liu and Chen (2015) under identical conditions ($\tau_T = \tau_q = 0\ s$ and $G = w_b\rho_b C_b$), as shown in Fig. 2(e). The result shows the good excellent between present study and literature data. These results support the reliability and precision of the PBH, DPL and LTNE models for simulating the temporal thermal response of biological tissue.

The next section presents a comparative analysis of the thermal responses predicted by three bioheat transfer models: the Pennes bioheat model (PBH), the generalized dual-phase-lag model (DPL), and the local thermal non-equilibrium model (LTNE). This study aims to analyze temperature evolution and thermal damage during microwave ablation (MWA) under varying heating time (t_p) and tissue porosity levels (ε). In this study, the heat source of the MWA was modeled as a constant heat flux (q_0), with heating time of 5 and 20 s. Table 1 summarized the thermal properties and parameters employed (Liu and Chen, 2015; Zeinali et al., 2024). Tissue porosity values of 0.0079, 0.0845, 0.1437, and 0.2165 were selected to represent different vascular structures. These porosity values directly affect the coupling factor (G) and phase lag times (τ_q and τ_T), which were calculated and were presented in Table 2.

Table 1
Parameters used in present study.

	Tissue	Blood	Reference
Thermal conductivity, k ($W/m\,K$)	0.628	0.5	Zeinali et al. (2024)
Heat capacity, C ($\mathrm{J}/kg\,K$)	4187	3860	Zeinali et al. (2024)
Density, ρ (kg/m^3)	1000	1060	Zeinali et al. (2024)
Metabolic heat generation, Q_{met} (W/m^3)	1.19×10^{-3}	–	Zeinali et al. (2024)
Tissue length, L (m)	5×10^{-2}	–	Zeinali et al. (2024)
Heat flux, q_0 (W/m^2)	19,000		Liu and Chen (2015)
Initial Temperature (°C)	37		

3.2. PBH, DPL, and LTNE models

Hyperthermia treatment involves biological tissues with complex microvascular systems, requiring appropriate heat transfer models to accurately predict their thermal behavior. Each bioheat model was developed based on specific physiological and physical assumptions that influence how tissue heating and cooling are represented. In Sections 3.2–3.5, simulations were restricted to temperatures below 100 °C to ensure physiological relevance and to avoid the effects of water evaporation and mechanical deformation, including tissue shrinkage and thermal denaturation.

Fig. 3(a and b) illustrates the temperature profiles predicted by the PBH, DPL, and LTNE models at a tissue porosity of 0.0845 for different heating times (t_p) of 5 and 20 s, respectively. In both cases, all models exhibited a sharp initial temperature rise during the heating phase, followed by a gradual cooling phase. Although there are no differences in the temperature rise, distinct behaviors appear during the cooling phase due to the different cooling mechanisms of each model. The DPL model, which incorporates factors such as phase lag, blood perfusion, and internal heat exchange between tissue and blood, demonstrates superior cooling performance for heating times (t_p) of 5 and 20 s. The PBH and LTNE models showed similar trends with only minor deviations. The temperature magnitudes at the end of heating showed slight differences for $t_p = 5$ s but became more pronounced for $t_p = 20$ s. The results emphasize that even at the same porosity level, model-specific assumptions strongly influence heat transport dynamics in biological tissue. Overall, these underscore the importance of tissue-blood heat exchange and phase lag effects in thermal responses of biological tissue, which are critical for predicting temporal temperature of tissue during hyperthermia.

3.3. Effect of tissue porosity, coupling factor, and phase lag time

The tissue porosity (ε), defined here as the fraction of void space in tissue associated with vascular and extravascular structures as shown in Fig. 1(a), was examined with emphasis on its effects on thermal parameters, coupling factors, phase lag times, and temperature evolution. As shown in Eqs. (5) and (6), porosity directly influences both the

Table 2
Coupling factors and phase lag times.

Porosity	d_b (mm)	h_b (W/ m^{2}K)	a_b (1/m)	$h_a a_b$ (W/ m^{3}K)	ρ_b (kg /m^3)	C_b (J /kg K)	ω_b (1/s)	$\rho_b C_b \omega_b$ (W/ m^{3}K)	G (W/ m^{3}K)	τ_q (s)	τ_T (s)
0.0079	4.56	540.5702	6.929825	3746.056	1060	3860	0.0064	26186.24	29932.296	1.0716	1.0731
0.0845	4.56	540.5702	74.12281	40068.58	1060	3860	0.0064	26186.24	66254.819	4.7866	4.8611
0.1437	4.56	540.5702	126.0526	68140.29	1060	3860	0.0064	26186.24	94326.533	5.3551	5.4986
0.2165	4.56	540.5702	189.9123	102660.9	1060	3860	0.0064	26186.24	128847.15	5.4133	5.6353

Table 3
Study of maximum time step on temperature for present simulations.

Maximum time step, Δt_{max} (s)	PBH Model	DPL Model	LTNE Model	
			Tissue phase	Blood phase
$\Delta t_{max} = 1.00$ s	47.961	47.403	47.969	45.439
$\Delta t_{max} = 0.5$ s	47.961	47.404	47.970	45.440
$\Delta t_{max} = 0.1$ s	47.963	47.405	47.971	45.441
$\Delta t_{max} = 0.05$ s	47.963	47.405	47.971	45.441
$\Delta t_{max} = 0.01$ s	47.963	47.405	47.971	45.441

Table 4
Mesh convergence analysis for present simulations.

Size of mesh, Δx (m)	Temperature ($^\circ C$) at 0.0025 m			
	PBH Model	DPL Model	LTNE Model	
			Tissue phase	Blood phase
1×10^{-2}	54.089	51.346	53.418	37.035
1×10^{-3}	47.961	47.276	47.886	45.132
1×10^{-4}	47.963	47.405	47.970	45.441
1×10^{-5}	47.963	47.405	47.971	45.411
5×10^{-6}	47.963	47.405	47.971	45.411
1×10^{-6}	47.963	47.405	47.971	45.411

coupling factor and the phase lag times. These parameters were used to characterize the rate of thermal response and the efficiency of interstitial convective heat transfer between the tissue and blood phases. The phase lag times of temperature gradient (τ_T) and heat flux (τ_q) were summarized in Table 2. From these calculations, it observed that higher porosity typically leads to longer phase lag times and a greater heat transfer coefficient between tissue and blood. Increased porosity also reflects a larger interfacial area (a_b) between vascular and extravascular regions, thereby enhancing the heat-exchange efficiency within biological tissue.

Fig. 3(c and d) illustrates the effect of tissue porosity ($\varepsilon = 0.0079, 0.0845, 0.1437,$ and 0.2165) on temperature evolution for heating time $t_p = 5$ and 20 s at V = 0.1 mm/s. Overall, the simulations show that porosity strongly influences the temporal temperature profile during both heating and cooling, particularly in the LTNE and DPL models where tissue-blood heat exchange is explicitly governed by tissue porosity (ε). The maximum temperature of all cases was presented in Fig. 3(e and f). In the LTNE model, higher porosity consistently reduced the peak temperature during heating phase, as the greater vascular region produces more convective cooling and heat removal within tissue. In contrast, the DPL model revealed more complex response. For $t_p = 5$ s, increased tissue porosity elevated the maximum temperature (see Fig. 3 (e)). For $t_p = 20$ s, the trend reversed, with peak temperature decreasing as porosity increased (see Fig. 3(f)). These contrasting behaviors can be attributed to the interaction between tissue porosity and the phase lag effect, which is related to value of phase lag times of temperature gradient (τ_T) and heat flux (τ_q) (Afrin et al., 2012; Liu and Chen, 2015; Zeinali et al., 2024). Moreover, the duration of heating itself emerges as a critical determinant of the thermal response within the DPL framework, underscoring the sensitivity of the DPL model in hyperthermia treatment.

To further highlight the differences between the LTNE and DPL models, Fig. 3(g and h) presents the temporal temperature differences (ΔT = LTNE – DPL) for the same porosity, heating durations, and blood velocity (V = 1 mm/s). For short heating ($t_p = 5$ s), ΔT remains largely negative (≈ 0 to $-2.5\,^\circ C$) during the heating phase (Fig. 3(g)), indicating that DPL predicts higher tissue temperatures than LTNE across all porosity levels. For long heating ($t_p = 20$ s), ΔT is also negative for most porosities. However, it becomes positive ($\approx +2\,^\circ C$) near the end of heating at $\varepsilon = 0.0079$ (see Fig. 3(h)), showing that LTNE can predict higher temperatures under low-porosity conditions. After the heating period, ΔT gradually increases and eventually becomes positive in all cases, reflecting that DPL cools tissue more rapidly than LTNE due to the stronger influence of phase lag and coupling effects. This outcome is consistent with the definition of the coupling factor: in the DPL model, $G = h_b a_b + \rho_b C_b \omega_b$ which includes both the interfacial heat transfer coefficient and the blood perfusion. Whereas in the LTNE model, $G = h_b a_b$ account only for interfacial exchange. Consequently, DPL represents stronger convective dissipation within vascularized tissue, leading to faster cooling predictions than LTNE.

Since the LTNE framework explicitly calculates blood-phase temperature, Fig. 4(a and b) illustrates the spatial distribution of blood temperature along tissue length at different times. Interestingly, the peak blood temperature occurred a few seconds after the heating ended, in contrast to the tissue temperature response. For $t_p = 5$ s, the peak blood temperature was reached at approximately 8 s (see Fig. 4(a)), whereas for $t_p = 20$ s the peak shifted to around 24 s (see Fig. 4(b)). This delayed response indicates that blood continues to absorb heat from the surrounding tissue during hyperthermia treatment, resulting in a gradual increase in its temperature. These results reveals that in the LTNE model, porosity influences not only the magnitude of the peak tissue temperature but also the blood temperature. The peak magnitude subsequently decreases over time due to the ongoing heat exchange between the blood and tissue phases, which represents a heat transport within biological tissue under LTNE framework.

Fig. 5 presents the effect of porosity on blood temperature distribution along the tissue length. As discussed earlier, the peak blood temperature occurred at specific times after heating ended; therefore, 8 s and 24 s were selected to illustrate the influence of porosity on the maximum blood temperature. The results demonstrate that higher porosity consistently leads to lower maximum blood temperatures across all cases, consistent with the trends observed for maximum tissue temperature. The deviations became more pronounced under long heating conditions ($t_p = 20$ s) as shown in Fig. 5(b and d), whereas short heating ($t_p = 5$ s) produced only minor differences in maximum blood temperature as shown in Fig. 5(a and c). Therefore, the LTNE framework revealed a delayed temperature rise in the blood phase, reflecting the vascular thermal response during the hyperthermia therapy, which arises from the explicit calculation of blood temperature.

Consequently, these findings imply that tissues with higher vascular density (higher porosity) enhanced convective heat removal, whereas poorly vascularized tissues are more vulnerable to overheating. Moreover, the sensitivity of thermal predictions to porosity, phase lag, and coupling factors underscores their importance as physiological determinants of tissue thermoregulation. The results emphasize that ε, τ, and G must be carefully considered, as they directly affect the prediction of temperature distribution during hyperthermia treatment.

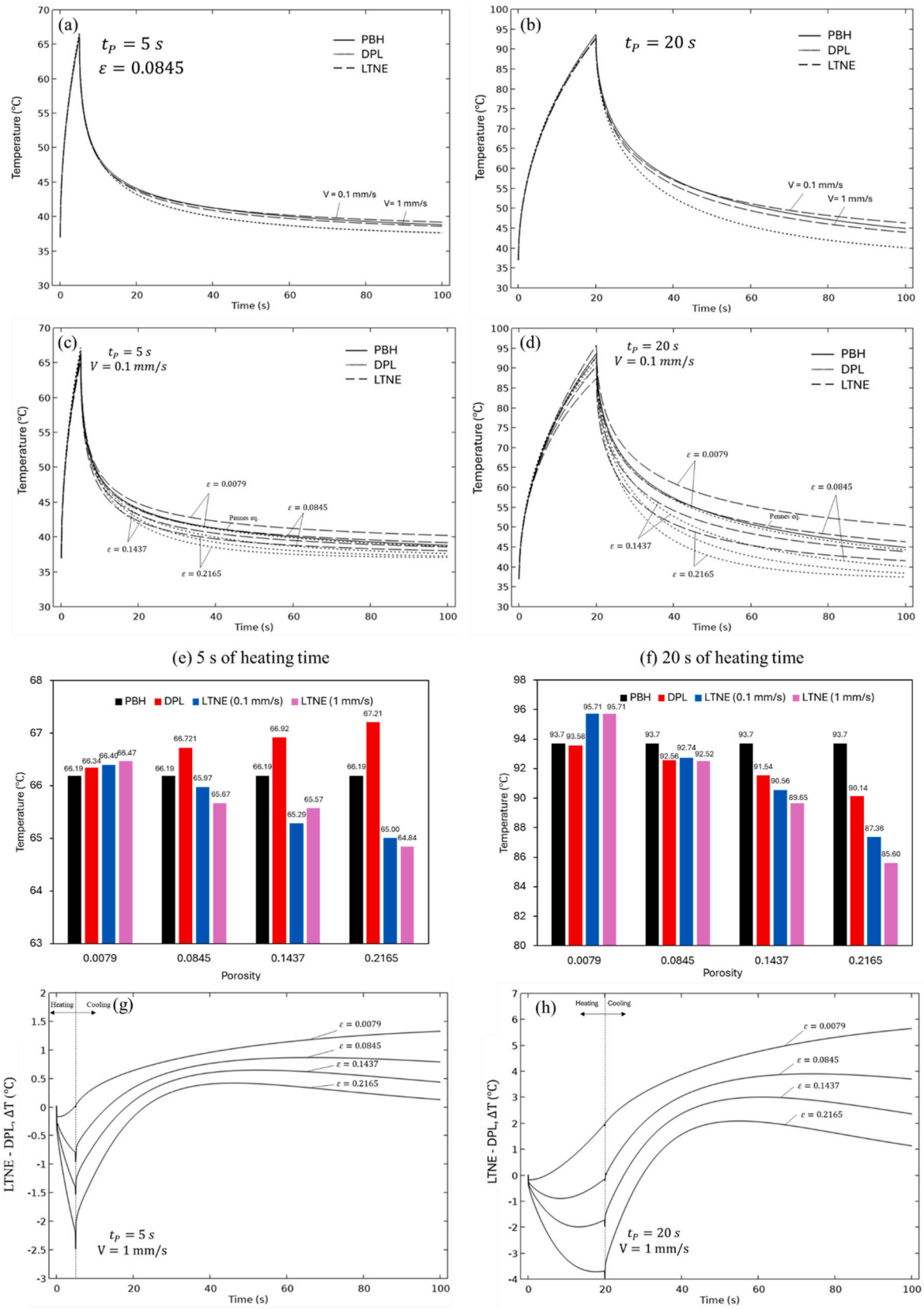

Fig. 3. Comparison of PBH, DPL, and LTNE models in predicting temperature evolution under different heating durations. (a) $t_p = 5$ s and (b) $t_p = 20$ s for a tissue porosity of $\varepsilon = 0.0845$. Effect of tissue porosity (ε) on the temperature evolution predicted by the PBH, DPL, and LTNE models for a blood velocity of $V = 0.1$ mm/s under different heating durations: (c) $t_p = 5$ s and (d) $t_p = 20$ s. Comparison of maximum temperatures predicted by the three models at various porosity levels for: (e) $t_p = 5$ s and (f) $t_p = 20$ s. Temporal temperature differences $(\Delta T = \text{LTNE} - \text{DPL})$ under different heating durations: (g) $t_p = 5$ s and (h) $t_p = 20$ s.

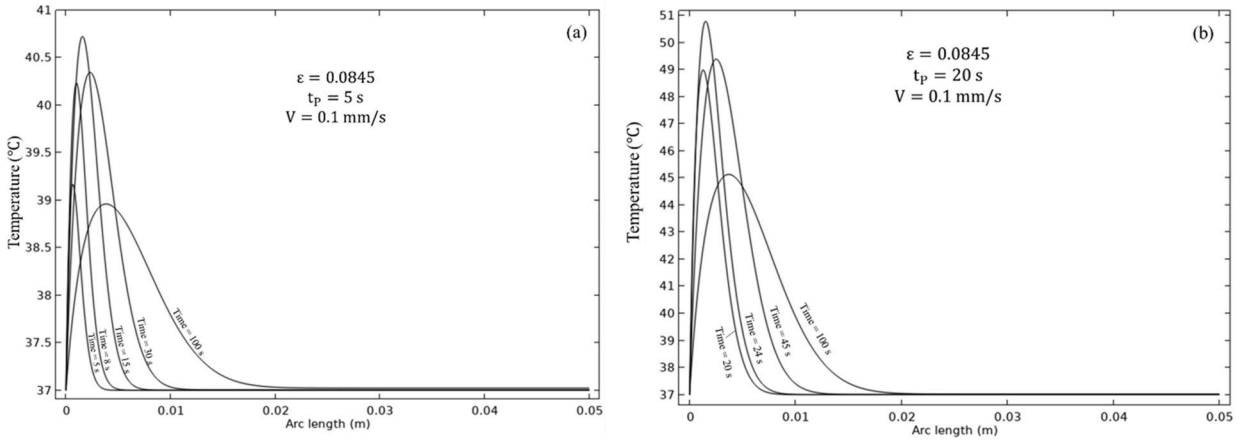

Fig. 4. Comparison of spatial distributions of blood temperature along the tissue length under different heating times: (a) $t_p = 5$ s and (b) $t_p = 20$ s.

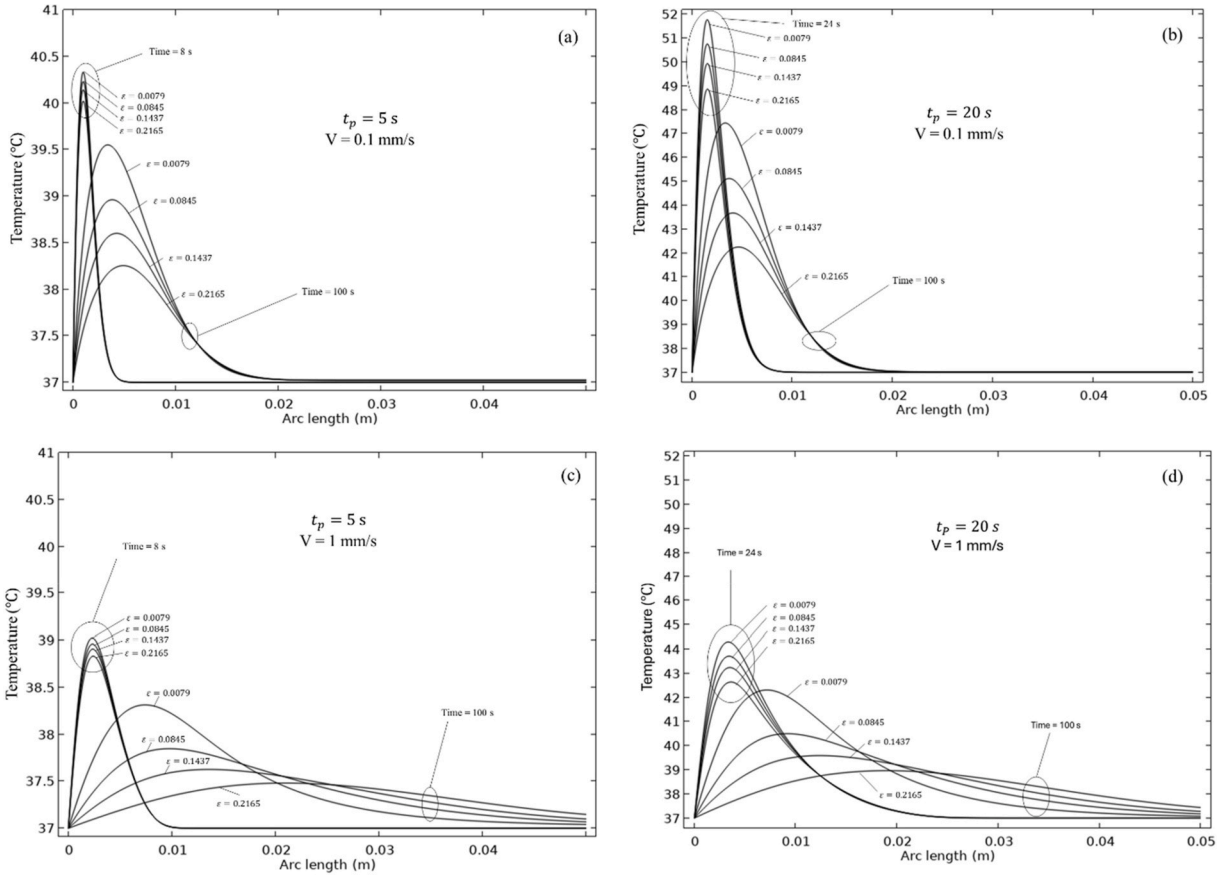

Fig. 5. Effects of tissue porosity (ε) on the spatial distributions of blood temperature under different heating times (t_p) and blood velocities (V): (a) $t_p = 5$ s, V = 0.1 mm/s; (b) $t_p = 20$ s, V = 0.1 mm/s; (c) $t_p = 5$ s, V = 1 mm/s; and (d) $t_p = 20$ s, V = 1 mm/s.

3.4. Effect of blood velocity

As previously discussed, the transient behavior of blood temperature can be explicitly captured in the LTNE model, providing valuable insight into tissue–blood thermal interactions. This section investigates the effects of blood velocity on heat transfer within tissue during hyperthermia treatment. In this study, the blood flow velocity is interpreted as a representation of two important physiological phenomena. First, it accounts for the baseline internal blood perfusion, which refers to the natural microvascular flow (Yuan, 2008). Second, it captures the thermally induced variation in blood velocity that occurs when tissue temperature rises during hyperthermia therapy (Keangin and Rattanadecho, 2018; Preechaphonkul and Rattanadecho, 2021; Wessapan and Rattanadecho, 2023).

Fig. 3(a and b) demonstrates that a higher velocity (V = 1 mm/s) reduces tissue temperature more effectively than a lower velocity (V = 0.1 mm/s) as observed in cooling phase. The impact of blood velocity size on the maximum tissue temperature was illustrated in Fig. 3(e and f). No clear pattern was observed for $t_p = 5$ s (see Fig. 3(e)), and the maximum temperature appeared irregular across different tissue porosities. When the heating time $t_p = 20$ s, a distinct trend became apparent. The higher blood velocity (V = 1 mm/s) consistently led to

lower maximum temperatures, as indicated in Fig. 3(f). Moreover, higher blood velocity (V = 1 mm/s) reduces the magnitude of blood temperature. For $t_p = 5$ s, the blood temperature decreased by approximately 1–1.5 °C (see Fig. 5(a and c)), whereas for $t_p = 20$ s, the reduction reached about 8–9 °C, depending on the level of tissue porosity (see Fig. 5(b and d)). Blood velocity also strongly affects the spatial distribution of blood temperature along the tissue length as shown in Fig. 5. At lower velocity (V = 0.1 mm/s), it was observed that heated blood remains near the heating site due to slow blood flow, leading to localized retention of thermal energy. In contrast, at higher velocity (V = 1 mm/s), blood rapidly transports heat away from the heated zone, which can elevate the temperature and damage area of surrounding tissues (See Fig. 6(a and b)).

Although the rise in blood temperature was modest in this study, this phenomenon is expected to become more pronounced during hyperthermia treatments of longer duration, which significantly increase tissue temperature and induce blood velocities. These effects intensify the convective transport of heat within the vascular domain, as represented by the term $\rho_b C_b V \cdot \nabla T_b$ in the LTNE Model. As mentioned earlier, this convective term represents the blood flow that occurs in response to a temperature increase, with the flow direction following the path of heat transport. This behavior reflects the physical mechanism of thermally driven blood motion within the vascular region, distinguishing the LTNE model from the PBH and DPL models, which neglect this convective coupling between blood flow and temperature distribution. Therefore, LTNE modeling incorporating blood convection should not be overlooked when simulating or optimizing thermal treatments in biological tissues.

3.5. Thermal damage

In hyperthermia therapy, the thermal damage area is a key indicator of treatment effectiveness. This section investigates the thermal damage areas predicted by the three models considered in this study. The simulation results indicate that the PBH, DPL, and LTNE models produce significantly different thermal damage predictions for the treatment of hyperthermia. Fig. 6(a and b) demonstrates the comparative study of a fraction of necrotic tissue (θ_d) across models for $\varepsilon = 0.0845$ and $t_P = 20$ s. The LTNE model predicted the largest thermal damage zone, followed by PBH, while DPL produced the smallest. The difference became more pronounced at higher blood velocity. This is consistent with the trend of spatial blood temperature discussed in the previous section, highlighting the strong sensitivity of LTNE model predictions of thermal damage to blood velocity in hyperthermia treatment. In addition, thermal damage was strongly influenced by tissue porosity, as illustrated in Fig. 6(c). Increasing porosity reduced the necrotic fraction in both DPL and LTNE models. These results align with the temperature distributions discussed in Sections 3.3 and 3.4 and emphasize the importance of selecting an appropriate bioheat model for predicting both temperature evolution and thermal damage in hyperthermia treatment. Accurate prediction of the thermal damage zone is essential for optimizing treatment efficacy and ensuring patient safety.

3.6. Comparison with experimental data

As mentioned in previous section, finding the optimal bioheat model for hyperthermia treatment remains a challenge. Comparing simulation results with experimental data is crucial for identifying limitations and

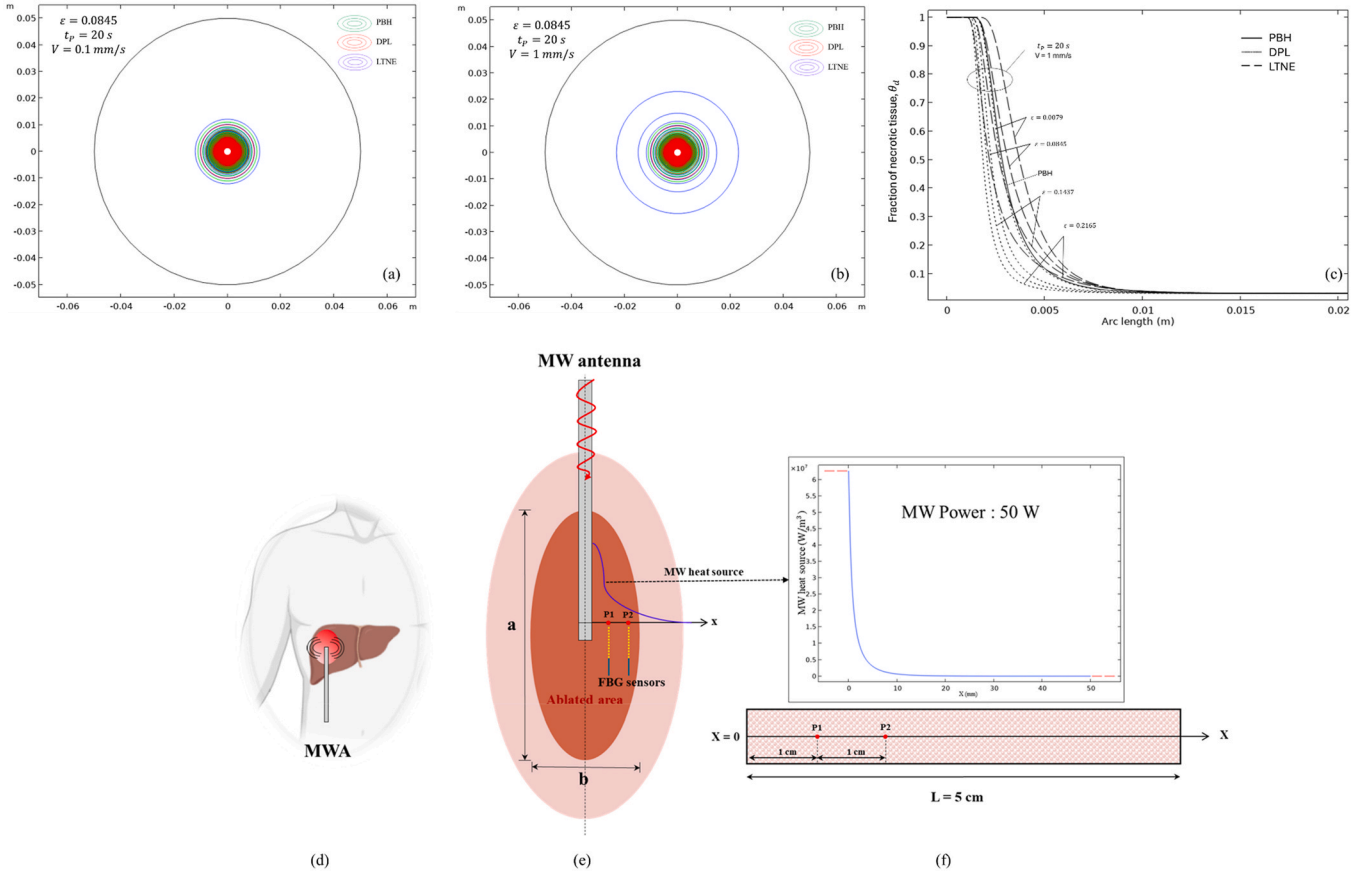

Fig. 6. Thermal damage contours predicted by the PBH, DPL, and LTNE models at $t_p = 20$ s for different blood velocities: (a) V = 0.1 mm/s and (b) V = 1 mm/s. (c) Effect of tissue porosity (ε) on the fraction of necrotic tissue (θ_d) along the tissue length. (d) Illustration of microwave ablation (MWA) in the human liver. (e) Schematic diagram of the ablation region during MWA with FBG sensors (P1 and P2) used for temperature monitoring. (f) Simplified one-dimensional model and volumetric heat distribution of microwave power for MWA treatment.

determining the most suitable model. Therefore, in this section, the experimental data obtained from Namakshenas et al. (2024) were used to compare the temperature evolution of the PBH, DPL, and LTNE models. In their experiment, single and double antennas were used to investigate the ablation axes of biological tissues, such as the liver, lungs, and kidneys during microwave ablation (MWA). The liver temperature and ablation axes of microwave ablation (MWA) using a single antenna with 50 W for 5 min, as collected by Namakshenas et al. were selected for this study. The schematic for Microwave Ablation (MWA), along with the experimental setup's Namakshennas et al. (2024) and a simplified one-dimensional model, was illustrated in Fig. 6(d and e). Using a constant heat flux may not accurately represent the heat source for MWA. Hence, as obtained by Keangin and Rattanadecho (2013), Fig. 6(f) shows the volumetric heat source for MWA at 50 W. In addition, water evaporation can occur during the heating process because MWA is a high-temperature process. Therefore, the heat loss due to water evaporation was considered, and the latent heat of vaporization is represented by an additional term in all models. This adjustment ensures a more realistic prediction of the evolution of tissue temperature in MWA.

$$Q_{evap} = \alpha \frac{dW(T)}{dt}, \tag{20}$$

$$\frac{dW(T)}{dt} = \frac{\partial W(T)}{\partial T}\frac{\partial T}{\partial t}, \tag{21}$$

where α is water latent heat constant, which is 2260 (kJ/kg), and $W(T)$ represents the water density, which is assumed to be a function of temperature introduced by Yang et al. (2007), as follows:

$$W(T) = 778 \times \begin{cases} 1 - \exp\left(\dfrac{T-106}{3.42}\right), T \le 103 \\ 0.03713T^3 - 11.47T^2 + 1182T - 40582, 103 < T \le 104 \\ \exp\left(\dfrac{80-T}{34.37}\right), T > 104 \end{cases}. \tag{22}$$

Therefore, the heat loss terms for PBH, DPL, LTNE models are expressed as follows:

$$Q_{evap} = \alpha \frac{dW(T)}{dt}. \tag{23}$$

Tissue phase:

$$Q_{evap} = (1-\varepsilon)\alpha \frac{dW(T)}{dt}. \tag{24}$$

Blood phase:

$$Q_{evap} = \varepsilon\alpha \frac{dW(T_b)}{dt}. \tag{25}$$

By adding Eq. (23) to Eqs. (1) and (2), the PBH and DPL models were modified. Similarly, the LTNE model was modified by incorporating Eqs. (24) and (25) into Eqs. (9) and (10), respectively.

Meanwhile, the boundary conditions applied to all models are as follows:

Tissue phase:

$$(x = 0, L) - k\frac{\partial T}{\partial x} = 0. \tag{26}$$

Blood phase:

$$(x = 0, L) - k_b\frac{\partial T_b}{\partial x} = 0. \tag{27}$$

The initial temperature of liver in this comparison was set to 20 °C. The thermal properties of liver tissue used in validation against experiment data are $k = 0.497$ (W /m K), $\rho = 1030$ (kg /m^3), and $C = 3600$ (J /kg K) (Keangin et al., 2013). In addition, the blood perfusion rate, $\omega_b = 0.0036$ (1/s) and $Q_{met} = 0$ (W /m^3), and $\varepsilon = 0.1437$ were selected for this comparison. For the LTNE model, blood velocities of 0 mm/s, 0.05 mm/s, and 0.1 mm/s were selected to represent the extent range of blood flow velocities induced by the temperature increase. They were considered as representative values to illustrate average velocities due to high temperature induced blood flow to reveal its influence on temperature distribution and thermal damage prediction under LTNE conditions.

Fig. 7(a) shows a comparison of the temperature rise between Namakshenas et al.'s experiment and the present models of PBH, DPL, and LTNE at 1 and 2 cm. The results confirm that the LTNE (V = 0.05 mm/s) model provides the most precise and accurate prediction of temperature rise, whereas the DPL offers the least accuracy. The RSME was calculated to indicate the deviations between the present study and the results, as shown in Table 5. The RMSE values of the LTNE model at 1 and 2 cm were 1.16 °C and 0.90 °C, respectively, corresponding to percentage errors of 3.14 % and 17.05 %. The PBH model produced RMSE values of 5.98 °C and 3.04 °C, with percentage errors of 14.89 % and 57.71 %, while the DPL model showed the highest discrepancies, with RMSE values of 17.67 °C and 8.32 °C, and percentage errors of 41.84 % and 237.92 %, respectively. From the results, it is evident that the phase lag effect in the DPL model influenced the predicted temperature profiles, leading to largest deviations throughout the heating period. The DPL model exhibited the largest deviation from the experimental data, which can be attributed to the inherent difficulty of

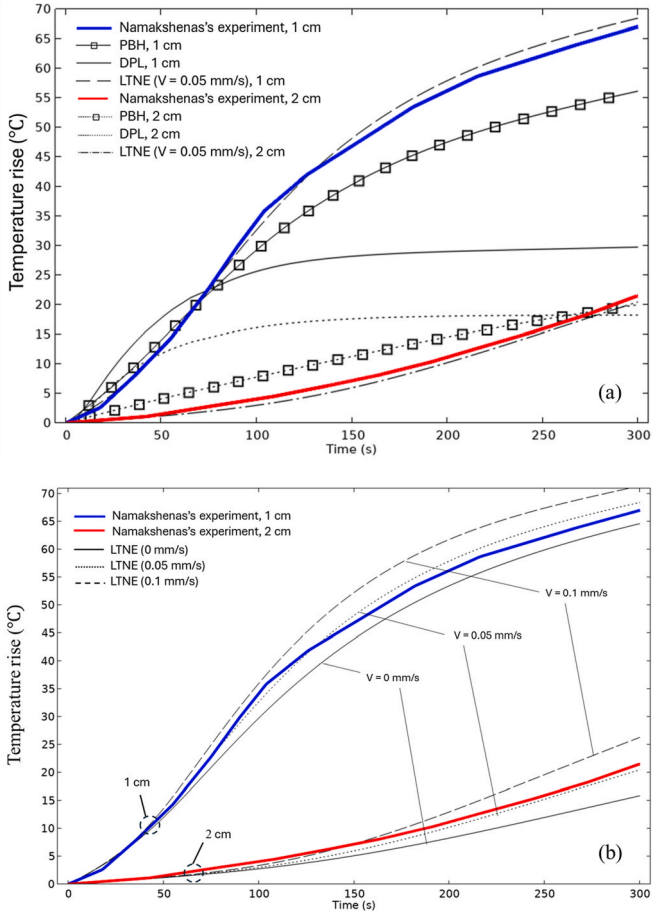

Fig. 7. (a) Comparison of temperature rise between the present models (PBH, DPL, LTNE (V = 0.05 mm/s) and experimental data from Namakshenas et al. at 1 cm and 2 cm using the single microwave antenna at 50 W for 5 min (ω_b = 0.0036 1/s, ε = 0.1437). (b) Effect of blood velocities on temperature rise in LTNE model compared to experimental data from Namakshenas et al. at 1 cm and 2 cm using the single microwave antenna at 50 W for 5 min (ε = 0.1437).

Table 5
Comparisons of RMSE of the liver tissue temperature between the present study and the experimental data reported by Namakshenas et al. (2024).

Position (mm)	Comparisons of RMSE with experimental data reported by Namakshenas et al. (2024) (°C)				
	PBH Model (Present study)	DPL Model (Present study)	LTNE Model (V = 0 mm/s) (Present study)	LTNE Model (V = 0.05 mm/s) (Present study)	LTNE Model (V = 0.1 mm/s) (Present study)
1 cm	5.98	17.67	3.49	1.16	2.79
2 cm	3.04	8.32	2.77	0.90	1.65

defining realistic phase lag times for biological tissues. Both the phase lag time of the temperature gradient (τ_T) and the phase lag time of the heat flux (τ_q) depend on multiple thermophysical and physiological parameters. During MWA with prolonged heating durations, these parameters are not constant because blood perfusion, heat transfer coefficients, and tissue properties continuously change with temperature rise, water evaporation, and tissue denaturation. Such variations inevitably alter the effective phase lag times as the process evolves. Therefore, assuming constant value of τ_T and τ_q throughout the heating period in the present study may lead to an underestimation of tissue temperature compared with the experimental data. In addition, the reported phase-lag times in biological tissues vary over a wide range depending on the modeling assumptions and experimental conditions (Azhdari et al., 2025). Consequently, the application of the DPL model with constant phase-lag times should be approached with careful consideration of these uncertainties and the underlying assumptions. Future work should further investigate time-dependent phase-lag formulations that can more accurately capture the dynamic physiological variations occurring during high-temperature ablation and validate them against experimental observations to determine realistic phase-lag times. In contrast, the PBH model shows smaller deviations than the DPL model. Nevertheless, the performance of the PBH model is strongly dependent on the blood perfusion rate parameter, which requires optimization to ensure physiologically realistic predictions. This highlights a key limitation of both the DPL and PBH models, as the accurate determination of phase lag times and blood perfusion rates is crucial, particularly for long transient processes such as MWA.

In addition, the effect of blood velocity in the LTNE model is illustrated in Fig. 7(b). The case of V = 0 mm/s represents the condition in which the convective term is neglected in the LTNE model. Under this condition, the predicted temperatures at both 1 cm and 2 cm are lower than the experimental data reported by Namakshenas et al. (2024), with RMSE values of 3.49 °C and 2.77 °C, respectively (see Table 5). This deviation occurs because the absence of blood convection toward the surrounding tissue leads to an underestimation of convective heat redistribution within the tissue and blood phases. When the blood velocity increases to V = 0.1 mm/s, the simulation shows that the temperatures at both 1 cm and 2 cm become higher than the experimental data, with RMSE values of 2.79 °C and 1.65 °C, respectively. This occurs because excessively high blood velocity transports more heat along the flow direction, resulting in unrealistic heat accumulation and limited local cooling. In contrast, the case of V = 0.05 mm/s provides the best overall agreement with the experimental results, yielding the lowest RMSE values as previously discussed. These findings highlight the importance of incorporating the convective term in hyperthermia modeling to account for blood convection, interstitial fluid transport, and water-vapor diffusion that occur during high-temperature treatments such as MWA. It also indicates that the representative blood-flow velocity values under the present conditions is approximately 0.05 mm/s on average.

In addition to the temperature comparison, the thermal damage area was also investigated to evaluate the predictive accuracy of the proposed model in estimating the extent of damage area observed the experimentally observed damage region. Fig. 8(a–c) illustrates the thermal damage contours predicted by the PBH, DPL, and LTNE models, respectively, under the same conditions as Namakshenas et al.'s experiment. In these figures, the yellow dashed line ($\theta_d = 1.0$) represents the zone of necrotic tissue, corresponding to fully thermally damaged tissue, while the white dashed line ($\theta_d = 0.43$) marks the minimum boundary of tissue where white coagulation occurs. These contours were used to compare ablated liver tissue and to highlight the discrepancies between the current models and the experimental data, which is shown in Fig. 8(d and e). From the comparison, the results indicate that the LTNE model predicted the largest ablation zone for fully damaged tissue ($\theta_d = 1.0$), followed by the PBH and DPL models. For the white coagulation zone ($\theta_d = 0.43$), the DPL model predicted the smallest area, whereas the PBH and LTNE models showed closer agreement with the experimental observations reported by Namakshenas et al. (2024).

Furthermore, the ablation axes predicted by present models were collected. Table 6 presents a comparison of ablation axes and areas in liver microwave ablation (MWA) between experimental results reported by Namakshenas et al. (2024) and present simulation results. The experimental values were observed as benchmarks, with reported ablation areas of 5.69 cm^2 and 9.84 cm^2 corresponding to two thermal damage thresholds, $\theta_d = 1.0$ (yellow dashed line) and $\theta_d = 0.43$ (white dashed line). Among the models evaluated, the PBH and DPL models significantly underestimate the ablation areas, with the DPL model performing the worst relative errors of −65.57 % and −54.07 % for the two thresholds. In contrast, the LTNE model exhibited smaller relative errors when compared with the experimental data. The LTNE model without blood flow (0 mm/s) achieves near-perfect accuracy at $\theta_d = 1.0$, with a relative error of +0.55 %. However, it underestimates the area at $\theta_d = 0.43$ with −17.32 %. At a blood velocity of 0.05 mm/s, the LTNE model slightly overestimates the area at $\theta_d = 1.0$ with +17.25 % and closely approximates the experimental result at $\theta_d = 0.43$ with −3.98 %. The LTNE model at 0.1 mm/s shows overestimation at $\theta_d = 1.0$ with +22.49 % and an excellent match at $\theta_d = 0.43$ with a relative error of just +1.07 %. Based on these results, it can be concluded that the blood convective term has a significant influence on the extent of the thermal damage area, especially in LTNE model, which is consistent with the findings discussed in previous sections.

Overall, the LTNE model closely matches experimental temperature profiles but slightly overestimates the extent of thermal damage compared to the observations reported by Namakshenas et al. (2024). The overestimation of the LTNE model, particularly in the fully damaged tissue region ($\theta_d = 1.0$), is mainly attributed to the absence of tissue shrinkage effects in the present simulations. In practice, liver tissue undergoes significant thermal contraction during MWA. Therefore, the ablation axes reported by Namakshenas et al. (2024) were measured after the tissue had already shrunk due to heating. Since the present model does not account for this mechanical deformation, the simulated ablation area appears larger than the experimental observation, even though the predicted temperature profiles show good agreement with the measured data. Similarly, Radosevic et al. (2021) also reported that simulation results tend to overestimate the experimental data. The observed differences between simulation and experimental results may be attributed to the limitations of the current models in accurately capturing the biomechanical deformation effects, such as thermal denaturation, tissue shrinkage, and carbonization that occur during the microwave ablation (MWA) process. Previous studies have investigated the shrinkage behavior of liver tissue under MWA, reporting that the ablation zone tends to shift toward the microwave antenna (Lee et al., 2022) and tissue contraction primarily occurs at the carbonized edge surrounding the thermally ablated region (Amabile et al., 2017). The extent of liver tissue shrinkage has been reported to range between approximately 10 %–40 %, depending on sample size and tissue composition (Farina et al., 2018). Recently, Che et al. (2025) conducted an MWA simulation that incorporated tissue shrinkage phenomena.

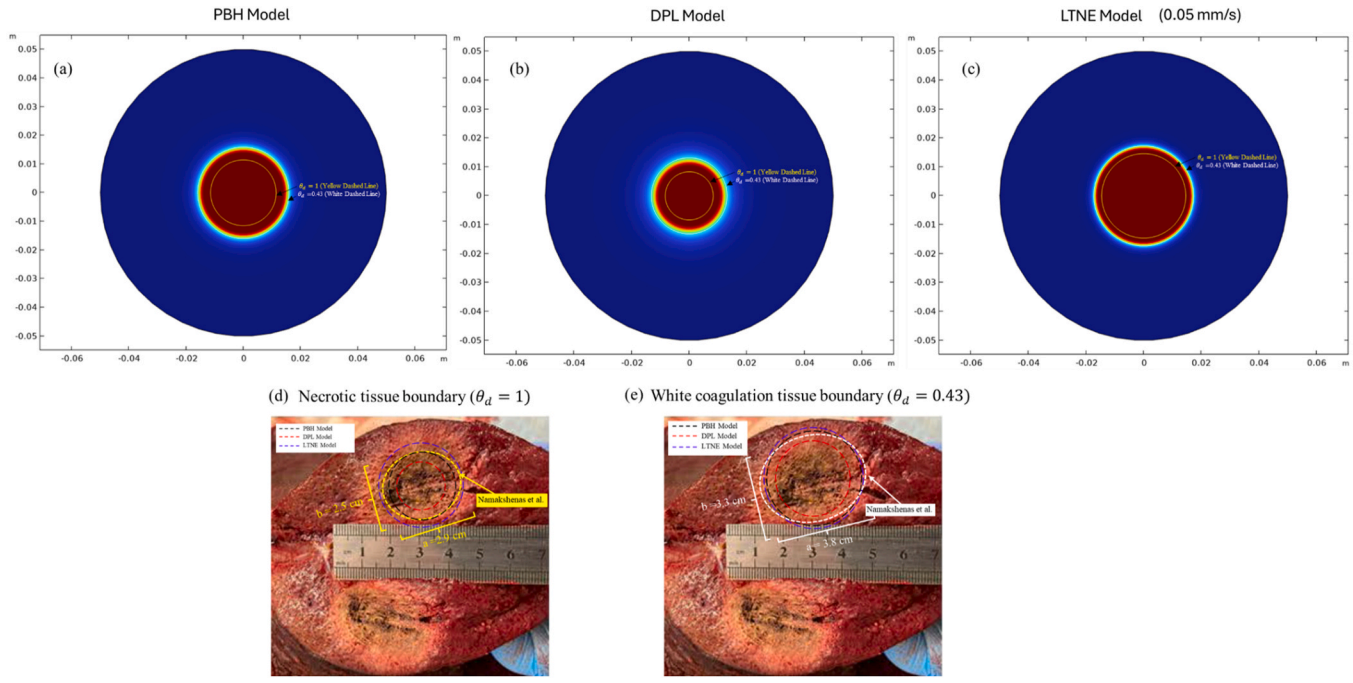

Fig. 8. Thermal damage area predicted by PBH (a), DPL (b), and LTNE (c), Ablation axes of a single-Antenna Microwave Ablation in Liver Tissue Observed by Namakshenas et al. (2024). The experimental image in Fig. 8(d and e) are adapted from "Performance of an Anti-Phase Technology-Powered Microwave Ablation System on Ex Vivo Liver, Lung and Kidney: Analysis of Temperature Trend, Ablation Size and Sphericity" by Pouya Namakshenas, Arcaini Tommaso, Cesare Benedetta, Dorato Alessandro, Durante Elena, Milena Ricci, Domiziana Santucci, Paola Saccomandi, and Elio aiella, under the Creative Commons Attribution (CC BY) License (https://creativecommons.org/licenses/by/4.0/(For interpretation of the references to color in this label legend, the reader is referred to the web version of this article.).

Table 6
Comparison of ablation axes of liver MWA of present models and data provided by Namakshenas et al. (2024).

MW setting, Single antenna (50 W, 5 min)	Ablation Axes $\theta_d = 1$ (Yellow dashed line)		Area (cm^2)	Ablation Axes $\theta_d = 0.43$ (White dashed line)		Areas (cm^2)	Relative Error (%) $\left(\frac{Area_{exp} - Area_{sim}}{Area_{exp}}\right) \times 100$	
	a (cm) (Experiment)	b (cm) (Experiment)		a (cm) (Experiment)	b (cm) (Experiment)		$\theta_d = 1$	$\theta_d = 0.43$
Namakshenas et al. (2024)	2.9	2.5	5.69	3.8	3.3	9.84	–	–
Present Study	a (cm) (Simulation)	b (cm) (Simulation)		a (cm) (Simulation)	b (cm) (Simulation)			
PBH Model	2.29	2.29	4.12	3.20	3.20	8.04	−24.47	−22.37
DPL Model	1.58	1.58	1.96	2.40	2.40	4.52	−65.57	−54.07
LTNE Model (0 mm/s)	2.70	2.70	5.72	3.22	3.22	8.14	+0.55	−17.32
LTNE Model (0.05 mm/s)	2.92	2.92	6.69	3.47	3.47	9.45	+17.25	−3.98
LTNE Model (0.1 mm/s)	3.16	3.16	7.84	3.75	3.75	11.04	+22.49	+1.07

Notes.
1.PBH Model: Pennes bioheat model.
2.DPL Model: Generalized dual-phase lag model.
3.LTNE Model: Local thermal non-equilibrium model.
4. $\theta_d = 1$, Complete necrosis of tissue.
5. $\theta_d = 0.43$, White coagulation zone in tissue.
6. The negative sign (−) indicates that the simulation predicts a smaller area, whereas the positive sign (+) represents a larger predicted area.

Their results demonstrated that tissue contraction caused the heated region to shift closer to the antenna. The exclusion of biomechanical responses in the present simulations may lead to an overestimation of the ablation zone, particularly within the fully damaged tissue and at the interface between the thermally affected and white coagulation regions. Accounting for tissue shrinkage, thermal denaturation, and carbonization is expected to yield a smaller, more realistic, and experimentally consistent prediction of the thermal damage extent.

It should be noted that the present analysis is limited to one-dimensional simulations, with validation performed against existing experimental data. The simplification adopted in this model, in which a one-dimensional domain was revolved to generate a two-dimensional axisymmetric geometry, also restricts the model's ability to represent the realistic ablation patterns. Experimental observations by Namakshenas et al. (2024) show that the ablation zone exhibits an elliptical or water-drop shape consistent with two-dimensional simulations (Wessapan et al., 2025; Che et al., 2025), differing from the circular profile predicted here. Moreover, temperature-dependent variations in

physical properties such as density, thermal conductivity, and specific heat can strongly influence energy transport processes, as can changes in dielectric properties that occur during the MWA procedure (Preechaphonkul and Rattanadecho, 2022). In contrast, the present study assumes constant material properties and a uniform volumetric heat source throughout the heating period. These effects are expected to become more pronounced under high-power and long-duration heating conditions, particularly in the LTNE model, which simultaneously governs the heat exchange between the tissue and blood phases.

The results also emphasize that both the magnitude and direction of blood-flow velocity are crucial determinants of bioheat transfer precision. The inclusion of the convection term in the LTNE model significantly enhances the accuracy of thermal-response predictions by providing a more realistic description of heat redistribution between the tissue and blood phases. However, the blood velocity used in comparison with experiment data was determined from several simulation trials rather than derived from Multiphysics coupling such fluid flow analysis. In MWA, blood velocity in biological tissue dynamically increases with temperature due to thermally induced expansion and perfusion but gradually decreases over time as evaporation, blood coagulation, and tissue denaturation occur (Preechaphonkul and Rattanadecho, 2021; Wongchadakul et al., 2023a,b; Wessapan et al., 2025). These variations alter the convective heat transfer rate and consequently influence both the spatial extent and the distribution of the temperature field. Because of the one-dimensional assumption, blood flow occurs in a single direction, restricting the model's ability to capture multidirectional convection that naturally develops in vascularized tissue. This simplification may therefore reduce the accuracy of the predicted temperature distribution and the estimated thermal damage area. Consequently, incorporating temperature-dependent or time-varying blood velocity fields within two- or three-dimensional LTNE models in future studies would enable a more realistic and accurate simulation of the coupled thermal–fluid dynamics that occur during hyperthermia treatments. In this study, a porosity value of 0.1437 was selected for comparison, since the exact porosity of the liver tissue in Namakshenas et al.'s experiment was not reported (Namakshenas et al., 2024). It was therefore assumed that blood-flow velocity depends on tissue porosity to achieve the best agreement with the experimental temperature data. Extending the LTNE model to examine a range of porosity values can provide deeper insight into how microstructural variations influence convective heat transfer and the extent of thermal damage, thereby improving the physical realism and predictive capability of the model.

Finally, the present model was developed primarily as a conceptual framework to conduct a comparative study and identify the most appropriate heat-transfer formulation for hyperthermia simulations. The findings reveal that the LTNE model is the most suitable among the three investigated models for thermal response prediction, though it still tends to overestimate the thermal damage area. Future developments should therefore extend the model to two- and three-dimensional domains and incorporate additional coupled phenomena, including tissue shrinkage, thermal denaturation, carbonization, and temperature-dependent property variations, and time-dependent blood velocity to enhance physiological relevance and predictive accuracy. Refining these predictive frameworks through such Multiphysics coupling will be essential for improving model reliability and optimizing hyperthermia treatment outcomes. The demonstrated predictive capability of the LTNE model in estimating temperature evolution and thermal damage suggests its potential for integration into preoperative planning as a simulation tool to optimize ablation parameters such as power input and heating duration for assessing therapeutic outcomes. To advance this framework toward clinical application, patient-specific information, including tumor size, geometry, and location; tissue thermophysical properties; and imaging data obtained from MRI or CT, should be incorporated for model construction and calibration. Validation under clinically relevant conditions will further ensure reliability and accuracy. With these enhancements, the LTNE-based framework could serve as a robust predictive tool to support personalized and effective hyperthermia and ablation treatment planning.

4. Conclusions

This study presented a comprehensive numerical investigation of heat transfer and thermal damage in biological tissue during microwave ablation (MWA). The analysis systematically compared three bioheat models consist of PBH, DPL, and LTNE under identical treatment conditions and examined the influence of key physiological and structural parameters, including porosity, blood velocity, coupling factor, and phase lag time. The present models were shown to be reliable, as their numerical results demonstrated excellent agreement with analytical solutions reported in the literature. The findings indicate that porosity strongly influences the thermal response of biological tissue, particularly in the DPL and LTNE models. Increasing tissue porosity enhances interfacial convective cooling withing vascularized tissue and reduces thermal damage. Blood velocity was identified as another critical factor in thermal regulation, with higher velocities lowering peak tissue but enlarging the thermal damage region. In addition, phase lag time and coupling factor were found to significantly affect temperature evolution, with pronounced effects observed in the DPL model. The PBH model provided a similar trend to the LTNE model at moderate porosity levels. Heating time was significant to temperature evolution especially in DPL. When validated against experimental data, the LTNE model provided the most accurate prediction of temperature rise and ablation area, achieving the lowest RMSE values of 1.16 °C and 0.90 °C at 1 cm and 2 cm, respectively, with corresponding percentage errors of 3.14 % and 17.05 %. In contrast, the PBH model yielded RMSE values of 5.98 °C and 3.04 °C (14.89 % and 57.71 %), while the DPL model showed the highest discrepancies, with RMSE values of 17.67 °C and 8.32 °C and percentage errors of 41.84 % and 237.92 %, respectively. Both the DPL and PBH models underestimated the temperature increase and ablation area, while the LTNE model slightly overestimated the ablation zone by +17.25 %, compared with −24.47 % and −65.57 % for the PBH and DPL models, respectively.

This outcome highlights the limitations of the DPL and PBH frameworks in selecting appropriate phase-lag times and blood perfusion rates. Meanwhile, the issue of the LTNE model overestimating thermal damage remains unresolved. Nevertheless, the LTNE framework can be considered the most appropriate among the three investigated models for temperature prediction, although its suitability for thermal damage estimation remains conditional upon further refinement to incorporate coupled thermal–mechanical effects. Future studies should therefore integrate additional mechanical and mass transport phenomena, such as tissue shrinkage, protein denaturation, water evaporation, and dynamic blood flow, to address these limitations. Extending LTNE formulations to two- and three-dimensional domains will further enhance their capability to represent realistic tissue geometries and spatial heat distributions. Consequently, the developed modeling framework can be extended to other thermal treatment modalities that share similar temperature ranges and underlying mechanisms, including water evaporation, natural convection, and tissue shrinkage. This addition reinforces the general applicability of the proposed framework to a broad range of hyperthermia and ablation therapies.

CRediT authorship contribution statement

Vannakorn Mongkol: Writing – review & editing, Writing – original draft, Validation, Software, Methodology, Investigation, Formal analysis, Data curation. **Phadungsak Rattanadecho:** Writing – review & editing, Resources, Project administration, Investigation, Funding acquisition, Conceptualization. **Wutipong Preechaphonkul:** Writing – original draft, Validation, Software, Formal analysis, Data curation. **Kambiz Vafai:** Writing – review & editing, Writing – original draft, Supervision, Project administration, Methodology, Investigation,

Formal analysis, Conceptualization.

Funding

This research project is supported by National Research Council of Thailand (NRCT): (Contact No. N41A640213), Thailand Science Research (TSRI) Fundamental Fund, fiscal year 2024, and Thailand Science Research (TSRI) Fundamental Fund, fiscal year 2025.

Declaration of competing interest

The authors declare that they have no known competing financial interests or personal relationships that could have appeared to influence the work reported in this paper.

Data availability

Data will be made available on request.

References

Abbas, I.A., El-Amin, M.F., Salama, A., 2009. Effect of thermal dispersion on free convection in a fluid-saturated porous medium. Int. J. Heat Fluid Flow 30 (2), 229–236. https://doi.org/10.1016/j.ijheatfluidflow.2009.01.004.

Abbas, I.A., Palani, G., 2010. Effects of magnetohydrodynamic flow past a vertical plate with variable surface temperature. Appl. Math. Mech. 31 (3), 329–338. https://doi.org/10.1007/s10483-010-0306-9.

Abbas, I., Hobiny, A., Alzahrani, F., 2020. An analytical solution of the bioheat model in a spherical tissue due to laser irradiation. Indian J. Phys. 94 (9), 1329–1334. https://doi.org/10.1007/s12648-019-01581-w.

Abbas, I.A., El-Bary, A.A., Mohamed, A.O., 2024. Generalized thermomechanical interaction in two-dimensional skin tissue using eigenvalues approach. J. Therm. Biol. 119, 103777. https://doi.org/10.1016/j.jtherbio.2023.103777.

Afrin, N., Zhou, J., Zhang, Y., Tzou, D.Y., Chen, J.K., 2012. Numerical simulation of thermal damage to living biological tissues induced by laser irradiation based on a generalized dual phase lag model. Numer. Heat Transf. A Appl. 61 (7), 483–501. https://doi.org/10.1080/10407782.2012.667648.

Alazmi, B., Vafai, K., 2000. Analysis of variants within the porous media transport models. J. Heat Tran. 122 (2), 303–326. https://doi.org/10.1115/1.521468.

Alzahrani, F.S., Abbas, I.A., 2019. Analytical estimations of temperature in a living tissue generated by laser irradiation using experimental data. J. Therm. Biol. 85, 102421. https://doi.org/10.1016/j.jtherbio.2019.102421.

Alzahrani, F.S., Abbas, I.A., 2021. Analytical solutions of thermal damage in living tissues due to laser irradiation. Waves Random Complex Media 31 (6), 1443–1456. https://doi.org/10.1080/17455030.2019.1676934.

Amabile, C., Farina, L., Lopresto, V., Pinto, R., Cassarino, S., Tosoratti, N., et al., 2017. Tissue shrinkage in microwave ablation of liver: an ex vivo predictive model. Int. J. Hyperther. 33 (1), 101–109. https://doi.org/10.1080/02656736.2016.1208292.

Amiri, A., Vafai, K., 1994. Analysis of dispersion effects and non-thermal equilibrium, non-Darcian, variable porosity incompressible flow through porous media. Int. J. Heat Mass Tran. 37 (6), 939–954. https://doi.org/10.1016/0017-9310(94)90219-4.

Andreozzi, A., Brunese, L., Iasiello, M., Tucci, C., Vanoli, G.P., 2019. Modeling heat transfer in tumors: a review of thermal therapies. Ann. Biomed. Eng. 47 (3), 676–693. https://doi.org/10.1007/s10439-018-02177-x.

Andreozzi, A., Brunese, L., Iasiello, M., Tucci, C., Vanoli, G.P., 2021. Numerical analysis of the pulsating heat source effects in a tumor tissue. Comput. Methods Progr. Biomed. 200, 105887. https://doi.org/10.1016/j.cmpb.2020.105887.

Andreozzi, A., Brunese, L., Iasiello, M., Tucci, C., Vanoli, G.P., 2022. Variable porosity-based bioheat model vs variable perfusion-based Pennes' equation: a comparison with in vivo experimental data. Therm. Sci. Eng. Prog. 35, 101469. https://doi.org/10.1016/j.tsep.2022.101469.

Antaki, P.J., 2005. New interpretation of Non-Fourier heat conduction in processed meat. J. Heat Tran. 127 (2), 189–193. https://doi.org/10.1115/1.1844540.

Azhdari, M., Rezazadeh, G., Pathak, R., Tautenhahn, H.M., Tautenhahn, F., Ricken, T., Seyedpour, S.M., 2025. A critical review of Non-Fourier heat transfer theories with phase lag in bio-heating: explaining the variations in reported phase lag coefficients. Int. J. Therm. Sci. 220, 110376. https://doi.org/10.1016/j.ijthermalsci.2025.110376.

Banerjee, A., Ogale, A.A., Das, C., Mitra, K., Subramanian, C., 2005. Temperature distribution in different materials due to short pulse laser irradiation. Heat Transf. Eng. 26 (8), 41–49. https://doi.org/10.1080/01457630591003754.

Boontatao, P., Pannucharoenwong, N., Sermlao, P., Panvichien, S., 2025. Generalized dual-phase-lag modeling of rectal wall thermal protection in prostate laser therapy using hyaluronic acid, collagen, and balloon spacers. Int. J. Heat Mass Tran. 253, 127570. https://doi.org/10.1016/j.ijheatmasstransfer.2025.127570.

Chabuanoi, T., Pannucharoenwong, N., Wongsangnoi, P., Rattanadecho, P., Saemathong, J., Hemathulin, S., 2024. Simulation effect of laser moving speed and spot size on maximum temperature in laser welding human skin tissue. Eng. Sci. 31, 1193. https://doi.org/10.30919/es1193.

Che, H., Lyu, J., Xu, E., Wu, J., 2025. Optimization and evaluation of liver deformation modeling under microwave ablation based on ex vivo data. Phys. Med. Biol. 70 (10), 105011. https://doi.org/10.1088/1361-6560/add07c.

Dombrovsky, L.A., Timchenko, V., Jackson, M., 2012. Indirect heating strategy for laser induced hyperthermia: an advanced thermal model. Int. J. Heat Mass Tran. 55 (17–18), 4688–4700. https://doi.org/10.1016/j.ijheatmasstransfer.2012.04.029.

Farina, L., Nissenbaum, Y., Cavagnaro, M., Goldberg, S.N., 2018. Tissue shrinkage in microwave thermal ablation: comparison of three commercial devices. Int. J. Hyperther. 34 (4), 382–391. https://doi.org/10.1080/02656736.2017.1362115.

Ghanmi, A., Abbas, I.A., 2019. An analytical study on the fractional transient heating within the skin tissue during the thermal therapy. J. Therm. Biol. 82, 229–233. https://doi.org/10.1016/j.jtherbio.2019.04.003.

Hobiny, A., Abbas, I., 2020. Thermal response of cylindrical tissue induced by laser irradiation with experimental study. Int. J. Numer. Methods Heat Fluid Flow 30 (8), 4013–4023. https://doi.org/10.1108/HFF-10-2019-0777.

Hobiny, A., Alzahrani, F., Abbas, I., 2020. Analytical estimation of temperature in living tissues using the TPL bioheat model with experimental verification. Mathematics 8 (7), 1188. https://doi.org/10.3390/math8071188.

Hobiny, A., Abbas, I., 2023. Influence of thermal relaxation time on thermomechanical interactions in biological tissue during hyperthermia treatment. J. Therm. Biol. 118, 103723. https://doi.org/10.1016/j.jtherbio.2023.103723.

Iasiello, M., Vafai, K., Andreozzi, A., Bianco, N., 2016. Low-density lipoprotein transport through an arterial wall under hyperthermia and hypertension conditions–An analytical solution. J. Biomech. 49 (2), 193–204. https://doi.org/10.1016/j.jbiomech.2015.12.015.

Iasiello, M., Andreozzi, A., Bianco, N., Vafai, K., 2020. The porous media theory applied to radiofrequency catheter ablation. Int. J. Numer. Methods Heat Fluid Flow 30 (5), 2669–2681. https://doi.org/10.1108/HFF-11-2018-0707.

Iasiello, M., Andreozzi, A., Bianco, N., Vafai, K., 2023. Effects of pulsed radiofrequency source on cardiac ablation. Bioengineering 10 (2), 227. https://doi.org/10.3390/bioengineering10020227.

Imanlou, S., Vafai, K., 2025. Analysis of magnetothermal hyperthermia on tumor ablation and Parkinson's therapy. Int. J. Heat Mass Tran. 254, 127697. https://doi.org/10.1016/j.ijheatmasstransfer.2025.127697.

Khanafer, K., Bull, J.L., Pop, I., Berguer, R., 2007. Influence of pulsatile blood flow and heating scheme on the temperature distribution during hyperthermia treatment. Int. J. Heat Mass Tran. 50 (23–24), 4883–4890. https://doi.org/10.1016/j.ijheatmasstransfer.2007.01.062.

Khaled, A.R., Vafai, K., 2003. The role of porous media in modeling flow and heat transfer in biological tissues. Int. J. Heat Mass Tran. 46 (26), 4989–5003. https://doi.org/10.1016/S0017-9310(03)00301-6.

Keangin, P., Rattanadecho, P., 2013. Analysis of heat transport on local thermal non-equilibrium in porous liver during microwave ablation. Int. J. Heat Mass Tran. 67, 46–60. https://doi.org/10.1016/j.ijheatmasstransfer.2013.07.064.

Keangin, P., Rattanadecho, P., 2018. A numerical investigation of microwave ablation on porous liver tissue. Adv. Mech. Eng. 10 (8), 1687814017734133. https://doi.org/10.1177/1687814017734133.

Keangin, P., Vafai, K., Rattanadecho, P., 2013. Electromagnetic field effects on biological materials. Int. J. Heat Mass Tran. 65, 389–399. https://doi.org/10.1016/j.ijheatmasstransfer.2013.06.039.

Klinger, H.G., 1974. Heat transfer in perfused biological tissue—I: general theory. Bull. Math. Biol. 36, 403–415. https://doi.org/10.1016/S0092-8240(74)80038-8.

Kotte, A.N.T.J., Van Leeuwen, G.M.J., Lagendijk, J.J.W., 1999. Modelling the thermal impact of a discrete vessel tree. Phys. Med. Biol. 44 (1), 57. https://doi.org/10.1088/0031-9155/44/1/006.

Kumar, P., Kumar, D., Rai, K.N., 2015. A numerical study on dual-phase-lag model of bio-heat transfer during hyperthermia treatment. J. Therm. Biol. 49, 98–105. https://doi.org/10.1016/j.jtherbio.2015.02.008.

Lee, J., Rhim, H., Lee, M.W., Kang, T.W., Song, K.D., Lee, J.K., 2022. Direction of tissue contraction after microwave ablation: a comparative experimental study in ex vivo bovine liver. Korean J. Radiol. 23 (1), 42. https://doi.org/10.3348/kjr.2021.0134.

Liu, K.C., Chen, H.T., 2015. Analysis of the bioheat transfer problem with pulse boundary heat flux using a generalized dual-phase-lag model. Int. Commun. Heat Mass Tran. 65, 31–36. https://doi.org/10.1016/j.icheatmasstransfer.2015.04.004.

Mahjoob, S., Vafai, K., 2009. Analytical characterization of heat transport through biological media incorporating hyperthermia treatment. Int. J. Heat Mass Tran. 52 (5–6), 1608–1618. https://doi.org/10.1016/j.ijheatmasstransfer.2008.07.038.

Mitchell, J.W., Myers, G.E., 1968. An analytical model of the counter-current heat exchange phenomena. Biophys. J. 8 (8), 897–911. https://doi.org/10.1016/S0006-3495(68)86527-0.

Mitra, K., Kumar, S., Vedevarz, A., Moallemi, M.K., 1995. Experimental evidence of hyperbolic heat conduction in processed meat. https://doi.org/10.1115/1.2822615.

Mohammadpour, M., Firoozabadi, B., 2020. High intensity focused ultrasound (HIFU) ablation of porous liver: numerical analysis of heat transfer and hemodynamics. Appl. Therm. Eng. 170, 115014. https://doi.org/10.1016/j.applthermaleng.2020.115014.

Namakshenas, P., Mojra, A., 2020. Microstructure-based Non-Fourier heat transfer modeling of HIFU treatment for thyroid cancer. Comput. Methods Progr. Biomed. 197, 105698. https://doi.org/10.1016/j.cmpb.2020.105698.

Namakshenas, P., Mojra, A., 2021. Optimization of polyethylene glycol-based hydrogel rectal spacer for focal laser ablation of prostate peripheral zone tumor. Phys. Med. 89, 104–113. https://doi.org/10.1016/j.ejmp.2021.07.034.

Namakshenas, P., Arcaini, T., Cesare, B., Dorato, A., Durante, E., Ricci, M., et al., 2024. Performance of an anti-phase technology-powered microwave ablation system on ex vivo liver, lung and kidney: analysis of temperature trend, ablation size and

Sphericity. Cardiovasc. Interv. Radiol. 47 (10), 1392–1401. https://doi.org/10.1007/s00270-024-03811-z.
Nakayama, A., Kuwahara, F., 2008. A general bioheat transfer model based on the theory of porous media. Int. J. Heat Mass Tran. 51 (11–12), 3190–3199. https://doi.org/10.1016/j.ijheatmasstransfer.2007.05.030.
Pennes, H.H., 1948. Analysis of tissue and arterial blood temperatures in the resting human forearm. J. Appl. Physiol. 1 (2), 93–122. https://doi.org/10.1152/jappl.1948.1.2.93.
Preechaphonkul, W., Rattanadecho, P., 2021. The comparative of the performance for predicted thermal models during microwave ablation process using a slot antenna. Case Stud. Therm. Eng. 25, 100908. https://doi.org/10.1016/j.csite.2021.100908.
Preechaphonkul, W., Rattanadecho, P., 2022. The effects of dielectric & thermal property functions on the thermal response during the focused microwave ablation treatment in the liver cancer model: numerical investigation. Eng. Sci. 21 (2), 788. https://doi.org/10.30919/es8e788.
Preechaphonkul, W., Mongkol, V., Sakonkanapong, A., Rattanadecho, P., 2025a. Numerical analysis of heat transfer and tissue deformation in liver cancer during microwave ablation: a comparison of bioheat and porous media models. Therm. Sci. Eng. Prog., 103739 https://doi.org/10.1016/j.tsep.2025.103739.
Preechaphonkul, W., Mongkol, V., Promoppatum, P., Srimaneepong, V., 2025b. Comparative analysis of repetitive pulsed and continuous laser heating in multi-layered skin: bioheat vs. dual-phase lag model perspective. Int. J. Thermofluids, 101371. https://doi.org/10.1016/j.ijft.2025.101371.
Radosevic, A., Prieto, D., Burdío, F., Berjano, E., Prakash, P., Trujillo, M., 2021. Short pulsed microwave ablation: computer modeling and ex vivo experiments. Int. J. Hyperther. 38 (1), 409–420. https://doi.org/10.1080/02656736.2021.1894358.
Rattanadecho, P., Keangin, P., 2013. Numerical study of heat transfer and blood flow in two-layered porous liver tissue during microwave ablation process using single and double slot antenna. Int. J. Heat Mass Tran. 58 (1–2), 457–470. https://doi.org/10.1016/j.ijheatmasstransfer.2012.10.043.
Reis, R.F., dos Santos Loureiro, F., Lobosco, M., 2016. 3D numerical simulations on GPUs of hyperthermia with nanoparticles by a nonlinear bioheat model. J. Comput. Appl. Math. 295, 35–47. https://doi.org/10.1016/j.cam.2015.02.047.
Roetzel, W., Xuan, Y., 1998. Transient response of the human limb to an external stimulust. Int. J. Heat Mass Tran. 41 (1), 229–239. https://doi.org/10.1016/S0017-9310(96)00160-3.
Shao, Y.L., Arjun, B., Leo, H.L., Chua, K.J., 2017a. A computational theoretical model for radiofrequency ablation of tumor with complex vascularization. Comput. Biol. Med. 89, 282–292. https://doi.org/10.1016/j.compbiomed.2017.08.025.
Shao, Y.L., Arjun, B., Leo, H.L., Chua, K.J., 2017b. Nano-assisted radiofrequency ablation of clinically extracted irregularly-shaped liver tumors. J. Therm. Biol. 66, 101–113. https://doi.org/10.1016/j.jtherbio.2017.04.005.
Silva, A.B.C., Wrobel, L.C., Ribeiro, F.L., 2018. A thermoregulation model for whole body cooling hypothermia. J. Therm. Biol. 78, 122–130. https://doi.org/10.1016/j.jtherbio.2018.08.019.
Singh, S., Melnik, R., 2020. Thermal ablation of biological tissues in disease treatment: a review of computational models and future directions. Electromagn. Biol. Med. 39 (2), 49–88. https://doi.org/10.1080/15368378.2020.1741383.
Suriyanto, Ng, E.Y.K., Kumar, S.D., 2017. Physical mechanism and modeling of heat generation and transfer in magnetic fluid hyperthermia through Néelian and Brownian relaxation: a review. Biomed. Eng. Online 16, 1–22. https://doi.org/10.1186/s12938-017-0327-x.
Tien, C.L., Vafai, K., 1989. Convective and radiative heat transfer in porous media. Adv. Appl. Mech. 27, 225–281. https://doi.org/10.1016/S0065-2156(08)70197-2.
Tucci, C., Trujillo, M., Berjano, E., Iasiello, M., Andreozzi, A., Vanoli, G.P., 2021. Pennes' bioheat equation vs. porous media approach in computer modeling of radiofrequency tumor ablation. Sci. Rep. 11 (1), 5272. https://doi.org/10.1038/s41598-021-84546-6.
Tucci, C., Trujillo, M., Berjano, E., Iasiello, M., Andreozzi, A., Vanoli, G.P., 2022. Mathematical modeling of microwave liver ablation with a variable-porosity medium approach. Comput. Methods Progr. Biomed. 214, 106569. https://doi.org/10.1016/j.cmpb.2021.106569.
Tzou, D.Y., 2014. Macro-to Microscale Heat Transfer: the Lagging Behavior. John Wiley & Sons.
Wang, K., Tavakkoli, F., Wang, S., Vafai, K., 2015. Analysis and analytical characterization of bioheat transfer during radiofrequency ablation. J. Biomech. 48 (6), 930–940. https://doi.org/10.1016/j.jbiomech.2015.02.023.
Weinbaum, S.J.L.M., Jiji, L.M., Lemons, D.E., 1984. Theory and experiment for the effect of vascular microstructure on surface tissue heat transfer—Part I: anatomical foundation and model conceptualization. https://doi.org/10.1115/1.3138501.
Wessapan, T., Rattanadecho, P., 2023. Flow and heat transfer through a porous tumor during high-intensity focused ultrasound. Int. J. Heat Mass Tran. 216, 124501. https://doi.org/10.1016/j.ijheatmasstransfer.2023.124501.
Wessapan, T., Keangin, P., Rattanadecho, P., Somsuk, N., 2025. Comparative analysis of heat transfer dynamics in high-intensity focused ultrasound and microwave ablation for cancer treatment. Int. J. Thermofluids, 101090. https://doi.org/10.1016/j.ijft.2025.101090.
Wongchadakul, P., Datta, A.K., Rattanadecho, P., 2023a. Tissue poromechanical deformation effects on steam pop likelihood in 3-D radiofrequency cardiac ablation. J. Biol. Eng. 17 (1), 52. https://doi.org/10.1186/s13036-023-00365-5.
Wongchadakul, P., Datta, A.K., Rattanadecho, P., 2023b. Natural convection effects on heat transfer in a porous tissue in 3-D radiofrequency cardiac ablation. Int. J. Heat Mass Tran. 204, 123832. https://doi.org/10.1016/j.ijheatmasstransfer.2022.123832.
Wulff, W., 2007. The energy conservation equation for living tissue. IEEE Trans. Biomed. Eng. (6), 494–495. https://doi.org/10.1109/TBME.1974.324342.
Yang, D., Converse, M.C., Mahvi, D.M., Webster, J.G., 2007. Expanding the bioheat equation to include tissue internal water evaporation during heating. IEEE (Inst. Electr. Electron. Eng.) Trans. Biomed. Eng. 54 (8), 1382–1388. https://doi.org/10.1109/TBME.2007.890740.
Yuan, P., 2008. Numerical analysis of temperature and thermal dose response of biological tissues to thermal non-equilibrium during hyperthermia therapy. Med. Eng. Phys. 30 (2), 135–143. https://doi.org/10.1016/j.medengphy.2007.03.006.
Zeinali, B., Mojra, A., Vafai, K., 2024. Analysis of HIFU thermal ablation for lung cancer incorporating local thermal non-equilibrium and non-fourier transfer. Int. Commun. Heat Mass Tran. 159, 108273. https://doi.org/10.1016/j.icheatmasstransfer.2024.108273.
Zhang, Q., Sun, Y., Yang, J., 2021. Thermoelastic behavior of skin tissue induced by laser irradiation based on the generalized dual-phase lag model. J. Therm. Biol. 100, 103038. https://doi.org/10.1016/j.jtherbio.2021.103038.
Zhang, Y., 2009. Generalized dual-phase lag bioheat equations based on nonequilibrium heat transfer in living biological tissues. Int. J. Heat Mass Tran. 52 (21–22), 4829–4834. https://doi.org/10.1016/j.ijheatmasstransfer.2009.06.007.
Zhou, J., Zhang, Y., Chen, J.K., 2009. An axisymmetric dual-phase-lag bioheat model for laser heating of living tissues. Int. J. Therm. Sci. 48 (8), 1477–1485. https://doi.org/10.1016/j.ijthermalsci.2008.12.012.

Glossary

a_b: Capillary surface area per unit tissue volume (m^2 /m^3)
A: Frequency factor (1/s)
Area: Damaged area (cm^2)
Bi: Biot number
C: Specific heat capacity of tissue (J/kg K)
C_b: Specific heat capacity of blood (J/kg K)
C_{sb}: Ratios of heat capacities of tissue and blood
d_b: vascular diameter (m)
E_a: Energy of activation of denaturation reaction (J/mol)
G: Coupling factors between blood and tissue (W/m^3 K)
h_a: Heat transfer coefficient of blood ($W/(m^2 \cdot K)$)
k: Thermal conductivity of tissue (W/m K)
k_b: Thermal conductivity of blood (W/m K)
k_{sb}: ratios of thermal conductivities of tissue and blood
L: Length (m)
Nu: Nusselt number
q_0: Heat flux (W/m^2)
Q_{evap}: Heat loss due to water evaporation (W/m^3)
Q_{ext}: External heat source term (W/m^3)
Q_{met}: Metabolic heat generation (W/m^3)
t: Time (s)
t_p: Heating time (s)
T: Tissue temperature (°*C*)
T_b: Blood temperature (°*C*)
T_0: Initial temperature (°*C*)
$W(T)$: Water content as a function of temperature (kg/m^3)
x: Spatial coordinate or space dimension (m)

Greek Symbols

α: Latent heat of vaporization of water (J/kg)
ρ_b: Density of blood (kg/m^3)
ρ_b: Density of blood (kg/m^3)
ω_b: Blood perfusion rate(1/s)
ε: Porosity
τ_q: Phase lag of heat flux (s)
τ_T: Phase lag of temperature gradient (s)
Ω: Cumulative tissue damage
θ_d: Fraction of damage

Subscript

b: Blood
d: Damage
eff: Effective property
evap: Evaporation
exp: Experiment
sb: Ratio between tissue and blood
sim: Simulation